

In-line Phase Contrast Tomography using  
Betatron X-rays Produced by a Laser-Plasma  
Accelerator

Master's Thesis  
Atomic Physics Department  
LTH, Lund, Sweden

*LRAP 536*

Kristoffer Svendsen

June 2017



**LUNDS UNIVERSITET**  
Lunds Tekniska Högskola

## Popular summary

Since the discovery of x-rays they have allowed us to see inside objects without the need to destroy, cut or damage them. This has been useful in many ways, foremost in the field of medicine where you can take images of the skeleton or other parts without the need of surgery. This works on the principle that x-rays penetrate objects more easily than visible light and it can penetrate deeper in skin for example. Denser objects are still harder to penetrate however, such as bone, and this leaves a shadow as fewer x-rays penetrate it. This also limits the technique in a way because it only allows you to see objects that are very dense compared to the surroundings, a bone surrounded by tissue for example. As such, it is not possible to see, say a tendon surrounded by tissue as they absorb about equal amounts of x-rays. This is where the technique of phase-contrast imaging comes in. It does not rely on how much x-rays the object absorbs, instead it relies on the difference in refractive index. As an example, say you have a piece of glass in water, both the glass and the water absorb about the same amount of x-rays so the glass would be hard to distinguish. But the refractive index of water compared to that of glass is quite different and taking phase-contrast images you would clearly be able to see the difference. This means that this technique has many useful applications but the problem is that it requires the source of the x-rays to be incredibly small, a few micrometers, and at the same time you need a lot of x-rays. This means that you either have to go to a synchrotron, which is very expensive and not always available, or use a microfocus x-ray tube that produces less x-rays.

In recent years a new type of particle accelerator has begun to catch the interest of a lot of researchers, called laser wakefield acceleration (LWFA). This uses a plasma to accelerate particles, usually electrons, over a very short distance. As a comparison, the linear accelerator at the MAX IV Laboratory accelerates electrons over 300 m, LWFA can reach the same energy over a distance of about 9 cm. The electrons emit x-rays when accelerated and this generates a very small x-ray source and was determined during this thesis to be 2.5 micrometers, which makes it suitable for phase-contrast imaging.

By rotating the object, taking images at different angles, one can reconstruct the full object in 3D even though the images are only 2D. Combining this with phase-contrast imaging makes it possible to create 3D images of small objects with little absorption. These 3D models can then be analyzed, such as cutting through different parts, rotating them, looking on the inside etc and this is demonstrated using a small fly in this thesis. Developing LWFA x-ray sources further could one day allow for phase-contrast imaging of for example blood vessels or tendons at medical facilities with very short exposure times compared to microfocus x-ray tubes. It would allow imaging of different low absorbing samples that usually require a synchrotron at much smaller and cheaper facilities.

## Abstract

X-ray phase-contrast imaging is a powerful technique that allows great resolving power for low absorbing samples such as biological tissue. This method relies on measuring the phase shift induced by the sample instead of the absorption traditional radiography relies on. This phase shift is measured as an intensity modulation at the detector and by using various algorithms one can obtain information about the sample. This technique can be combined with standard tomography to get a full 3 dimensional reconstruction of the sample.

Phase-contrast imaging requires a large transversal coherence, requiring a very small x-ray source size, limiting the choice of source to either microfocus x-ray tubes or a synchrotron facility. Microfocus x-ray tubes have very small source sizes but very limited flux, resulting in long exposure times while the beam time at a synchrotron facility is very expensive and limited. Laser based plasma acceleration could prove to be an alternative source for this purpose and this thesis dwell on this possibility, the source size is very small and the brilliance can be compared with that of a synchrotron. The generated x-ray pulses are also very short, on the femtosecond scale, reducing the exposure time needed for a well resolved image, resulting in faster data acquisition and holds promise for time resolved imaging. During the work presented in this thesis a source size measurement was conducted, showing a source size less than 2.5 microns, well suited for phase-contrast imaging. Experiments were carried out using low-absorbing samples such as mylar wires and a few different biological samples in the form of insects. The acquired phase-contrast images were used to calculate the projected thickness and by doing a tomography scan a full 3D reconstruction was created. In conclusion, this thesis shows laser based plasma accelerators to be a good source for phase-contrast imaging in low absorbing materials. Further, it proved to be able to resolve very small details, on the order of tens of microns and could possibly be improved further.

## Acknowledgements

I would like to thank all of the people involved in the process of this thesis. Namely Olle Lundh for his excellent supervision and guidance along with Martin Hansson, whose excitement encourages a person to new heights. I would also like to thank Isabel Gallardo Gonzalez for always having an answer to my questions, helping with the experimental setups, operation of the system, the long evenings of data acquisition and her overall involvement in the project. During this process I also shared an office with Hannes Pahl, whom repeatedly showed an interest in the project and led me in to many discussions that helped the project to evolve. I would also like to thank Elisa Rigosi from the Biologi Department at Lund University for providing us with some samples and helping in mounting the bee. Lastly I would like to thank my better half, Madeleine, that has been a great support, taking care of our son during late evenings and managing the home-field in general while I was occupied.

# Contents

<b>1</b>	<b>Introduction</b>	<b>1</b>
<b>2</b>	<b>Theory</b>	<b>5</b>
2.1	Laser Wakefield Acceleration . . . . .	5
2.1.1	X-ray generation . . . . .	8
2.2	X-ray Propagation . . . . .	10
2.2.1	Kirchhoff Diffraction . . . . .	11
2.2.2	Fresnel Diffraction . . . . .	12
2.2.3	Source Size Determination . . . . .	13
2.3	Phase Contrast . . . . .	16
2.3.1	In-line Phase Contrast . . . . .	17
2.3.2	Single material Phase Retrieval . . . . .	18
2.4	Tomography . . . . .	21
2.4.1	Radon Transformation . . . . .	22
2.4.2	Inverse Radon Transformation . . . . .	23
2.4.3	Filtered backprojection . . . . .	24
<b>3</b>	<b>Methodology</b>	<b>27</b>
3.1	Lund Multi-TW Laser . . . . .	27
3.2	Experimental Setup . . . . .	28
3.3	Source Size Determination . . . . .	31
3.3.1	Simulation . . . . .	32
3.4	Propagation and Phase-contrast Simulation . . . . .	34
3.5	Phase Contrast . . . . .	39
3.5.1	Numerical Implementation . . . . .	39
3.6	Alignment . . . . .	40
3.7	Tomography . . . . .	42
3.7.1	Numerical Implementation . . . . .	43
<b>4</b>	<b>Results</b>	<b>45</b>
4.1	Source Size Determination . . . . .	45
4.2	Phase Contrast . . . . .	48
4.3	Tomography . . . . .	49
4.4	3D Rendering . . . . .	54



# List of Figures

2.1	Electron binding potential . . . . .	6
2.2	D particle-in-cell simulation of LWFA . . . . .	7
2.3	Synchrotron radiation cone . . . . .	8
2.4	Wiggler radiation . . . . .	9
2.5	Energy spectrum . . . . .	10
2.6	Coordinate system for Kirchhoff diffraction . . . . .	11
2.7	Diffraction pattern smearing . . . . .	15
2.8	Method-of-choice flow chart . . . . .	19
2.9	Radon transformation . . . . .	22
2.10	Polar grid transformation to Cartesian . . . . .	24
2.11	Comparison of filtered and unfiltered backprojection . . . . .	26
3.1	Laser system scheme . . . . .	28
3.2	electron spectrum . . . . .	28
3.3	Experimental setup . . . . .	29
3.4	Experimental setup photograph . . . . .	30
3.5	Quantum efficiency curve . . . . .	31
3.6	Transmission of Beryllium and air . . . . .	32
3.7	Diffraction simulation for a tungsten wire, 10 micron . . . . .	34
3.8	Diffraction simulation for a tungsten wire, 50 micron . . . . .	35
3.9	2D diffraction simulation with projected thickness . . . . .	36
3.10	2D diffraction simulation with projected thickness with small magnification . . . . .	37
3.11	2D diffraction simulation with projected thickness, without noise and blur . . . . .	38
3.12	Photograph of fly specimen . . . . .	40
3.13	Alignment of reference object . . . . .	41
3.14	Centre of rotation . . . . .	42
3.15	Sinogram of a fly . . . . .	43
4.1	Fit of vertical source size . . . . .	46
4.2	Fit of horizontal source size . . . . .	47
4.3	Raw phase-contrast and projected thickness image of fishing line . . . . .	48
4.4	Raw phase-contrast and projected thickness image of a fishing line, reef knot . . . . .	49

4.5	Projected thickness of a fly . . . . .	50
4.6	Normalized projected thickness comparison . . . . .	51
4.7	Projected thickness image of a bee head . . . . .	51
4.8	Phase contrast image of a small fly . . . . .	52
4.9	Tomographic image of single knot fishing line . . . . .	52
4.10	Tomographic image of a bee's head . . . . .	53
4.11	Tomographic images of a fly . . . . .	53
4.12	3D rendering of a Reef knot . . . . .	54
4.13	3D rendering of a fishing line knot . . . . .	54
4.14	3D rendering of a fly's head . . . . .	55
4.15	3D rendering of a fly . . . . .	55
5.1	Electron beam profile for various laser polarization angles . . . . .	58
5.2	Filtered projected thickness . . . . .	58
5.3	Parallel and fan beam comparison . . . . .	60



# Chapter 1

## Introduction

Conventional x-ray imaging relies on the absorption of x-rays. For low-absorbing samples, that would be very small or thin samples for example, or a sample surrounded by another material with roughly the same absorption, this yields images of very low contrast. Phase-contrast imaging (PCI) gives a greater contrast in these cases as it relies on the phase change induced in the light field by a sample. This turns in to an intensity modulation that is measurable and is very sensitive to a change in refractive index, having the tendency to highlight edges of different materials. From these phase-contrast images, the phase of the light can be calculated and with this, the projected thickness. This can be used to do tomography, as this requires projection images, to obtain information on the sample in 3 dimensions. PCI requires a large coherence length [1], and this corresponds to a small source size, less than  $25\mu\text{m}$ . This technique thus requires beam time at a synchrotron that is expensive and not always available, or microfocus x-ray tubes with very limited flux, calling for extended exposure times [1]. Another type of particle accelerator that generates an x-ray source small enough to do PCI is a laser wakefield accelerator.

The interest in laser wakefield acceleration (LWFA) has increased in recent years as the performance of lasers have improved and is currently a topic of continues research. In these accelerators a high power laser beam is focused onto a gas target where the strong electrical field in the laser creates a plasma. The laser pulse then displaces electrons within this plasma, creating a "bubble" with no electrons. This results in very strong electric fields inside the plasma as there are local charge distributions. These regions, or bubbles, will propagate behind the laser close to the speed of light and inside them some electrons will be accelerated. The advantages of LWFA over conventional particle accelerators is the relative compactness of the system, consisting of a high powered laser, a vacuum chamber and a gas cell. The strong accelerating gradients inside the laser-generated plasma can reach up to  $1\text{ TV/m}$  [2], compared to that of a conventional radio frequency accelerator structures that is limited by electrical breakdown at  $100\text{ MV/m}$ . This reduces the acceleration distance significantly and the current record stands at an energy of  $4.2\text{ GeV}$  over a distance of 9

cm [3], compared to the linear accelerator at MAX IV, Lund, that reaches an energy of 3.7 GeV over a distance of 300 m [4]. Both LWFA and synchrotrons rely on the generation of x-rays from oscillating relativistic electrons, generating high intensity and well-directed x-ray beams. In a synchrotron this is done in insertion devices such as *wigglers* or *undulators* that consist of arrays of magnets of alternating polarity. After the electrons have been accelerated they are forced to oscillate due to these magnetic fields and thereby generate x-rays. In LWFA the electrons also oscillate and these oscillation are due to the focusing force of the plasma bubble, forcing any electrons off-axis to oscillate. As this is a natural part of the process in LWFA there is no need for external magnetic fields. The generated X-ray pulses from LWFA can have a brilliance comparable to third-generation synchrotrons [5] and are very short, on the order of femtoseconds [6].

The experimental setup to do propagation based phase-contrast imaging, also known as in-line phase-contrast imaging is very appealing as it requires no optical elements and is solely based on the free space propagation of the x-rays, making the technique easily implemented. The study of using LWFA for this purpose recently begun [1] - [7], and shows promising results. This thesis strives to show the possibility to generate fully 3D rendered volumes of low absorbing samples with  $\mu\text{m}$  resolution using a combination of phase-contrast imaging and tomography with x-rays generated by LWFA. Tomography works on the principle that, given projection images of a sample at different angles, one can reconstruct cross-sectional planes of the same sample. To view such a cross-sectional otherwise would mean cutting the sample in half, which may not always be preferable. The projection images are taken over 180 degrees using x-rays and as the absorption is connected to the material and geometry of the sample, this gives information about the objects structure. Using phase contrast imaging instead allow for imaging of low-absorbing samples and then, by calculating the projected thickness, one obtains information of the samples structure and this allows for a tomographic reconstruction.

To improve the contrast of the x-ray images, one would like to take the average of several shots at each angle. Due to laser pointing fluctuations, i.e. the focus of the laser moves slightly from shot-to-shot, the x-ray source will also move. This in turn means that the x-ray image will move so when taking the average the images will not be perfectly aligned. To do the full tomographic scan also takes some time and during this period the laser focus will have time to drift in a general direction. This will look like the object in the x-ray images are being moved so the reconstruction might be incorrect. To correct for this, one needs a way to align the images before taking the average and this can be done by using a reference object that is stationary and in the same plane as the sample. By aligning the images to this reference object they are also aligned with respect to the sample, thus correcting for laser pointing fluctuations and laser pointing drift.

The main goals of this thesis are:

- Measure the x-ray source size in the gas cell.
- Device a way to account for laser pointing fluctuations.
- Find a suitable phase retrieval algorithm and create phase-contrast images of a suitable sample.
- Create a tomographic reconstruction from the phase-contrast imaging and analyze the result.
- Create a 3D rendered image of the tomographic images.



# Chapter 2

## Theory

In this chapter, most of the theory needed to perform the experiments and analyze the results is presented. It gives a short introduction to laser wakefield acceleration, giving an understanding of the process and some of the characteristics of the generated x-rays. As diffraction is a big part of this thesis, the necessary theory is presented here along with a derivation of the phase-retrieval algorithm used. The theory of tomography is also included here, this is not strictly necessary as this was performed using pre-made algorithms. One should however have a basic understanding of the process and by applying this knowledge one can come to better conclusions analyzing the results.

### 2.1 Laser Wakefield Acceleration

This section is intended to be a brief introduction to laser wakefield acceleration. The PhD thesis "Controlled trapping in laser wakefield accelerators" by Martin Hansson [2] has been of great use in writing this section. This is not the main focus of this thesis but it does however require some basic knowledge to be able to understand some of the results.

When an atom is subjected to an external electric field the electrons binding potential undergoes a perturbation. A high electric field can decrease the binding potential enough to let bound electrons tunnel through it, as visualized in figure 2.1. If the electric field is very strong (as in the focus of a high power laser) the potential barrier becomes very low, allowing for electrons with binding energy above this threshold to escape its parent atom and if it is strong enough it can fully ionize the atom.

A gas can thus be ionized in this manner, using a high power laser to lower the binding potential and ionize the atoms, separating ions and electrons. This results in a region that, in total, has the same charge as the atoms before the ionization and is said to be quasi-neutral as there can be local charge distributions that are not neutral, this state of matter is generally referred to as a plasma.

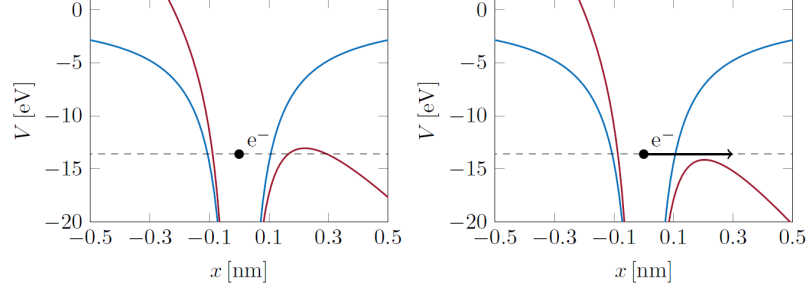


Figure 2.1: The Coulomb potential of the atom is shown in blue and is modified by an external electric field and the resulting total potential is shown in red. When this potential moves below the threshold, i.e. the binding energy of the electron the atom is ionized [2].

The propagation of light in a plasma is described by Maxwell's equation for a plane, monochromatic electromagnetic wave and can be written as

$$\begin{aligned} \vec{k} \times \vec{E} &= \omega \vec{B} \\ i\vec{k} \times \vec{B} &= \mu_0 \vec{j} - i\omega \mu_0 \epsilon_0 \vec{E} \end{aligned} \quad (2.1)$$

where  $\vec{k}$  is the wave vector,  $\vec{E}$  the electric field,  $\vec{B}$  the magnetic flux density and  $\omega$  the angular frequency of the electromagnetic wave.  $\mu_0, \epsilon_0$  are the permeability and permittivity in vacuum, respectively. The current density,  $\vec{j}$ , at low light intensities is approximately

$$\vec{j} = \frac{in_e e^2}{\omega m_e} \vec{E} \quad (2.2)$$

where  $n_e$  is the electron number density,  $e$  the elementary charge and  $m_e$  the electron rest mass.

It can be shown that for a light wave to be able to propagate through a plasma there exists a critical density

$$n_c = \frac{\omega^2 m_e \epsilon_0}{e^2} \quad (2.3)$$

above which it can no longer propagate[2]. A plasma above this density is therefore called an overdense plasma, and below it is called underdense.

In the ionized gas, i.e. the plasma, the ions can be considered stationary during the relevant time-frame in relation to the electrons as they are much heavier and move on a different timescale, making calculations and simulations easier.

When an electron interacts with an electromagnetic wave it will be the subject to the Lorentz force, which is

$$m_e \frac{\partial \vec{v}}{\partial t} = -e(\vec{E} + \vec{v} \times \vec{B}) \approx -e\vec{E} \quad (2.4)$$

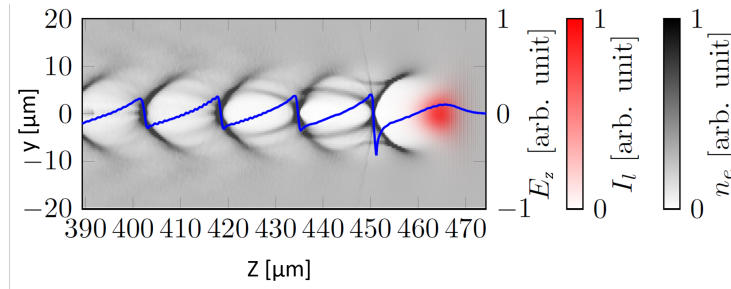


Figure 2.2: An image from a 3D particle-in-cell simulation of LWFA using the code CALDER-Circ. The laser pulse is shown in red, propagating from left to right, with the first plasma bubble trailing it. The gray-scale shows the electron density and the blue line shows the longitudinal electric field across the line  $y = 0$  across the wakes. These wakes will move with almost the same speed as the laser pulse and keep trailing it [2].

where  $\vec{v}$  is the electron velocity. This will induce an oscillatory motion to the electrons. This oscillation will not be completely symmetric as the amplitude of the electric field varies over the electron path, therefore the momentum gained in one direction will not be equal to that gained during the opposite direction of the oscillation and the electron will tend to drift towards regions of lower amplitude in the electric field. This is the background for what is called the *Ponderomotive force* and it looks like a short, focused laser pulse "pushes" the electrons out to the sides of the beam path. Due to restoring forces however, the electrons that have been pushed out will start accelerating back towards the low density region. Here, they will overshoot and continue past the optical axis and in towards a high density region again, and so it repeats. This oscillatory motion in the plasma is referred to as a plasma wave.

When the intensity of the laser pulse is sufficiently high the ponderomotive force will be strong enough to push out most of the electrons, leaving a void behind it. This is usually referred to as a *plasma bubble* or *blow-out regime*[2] and this creates strong gradients that can be used to accelerate electrons. Figure 2.2 shows an image from a 3D simulation, showing the electron density in grey and the laser pulse in red.

For an electron to be accelerated it has to somehow be injected into the plasma bubble as this is where the strong gradient exist. This can occur automatically if the plasma wave becomes too large in amplitude, the wave will then break as it loses coherence. During this process some electrons may be injected into the bubble and, if the wave does not break completely and retains some wave-like structure without being deformed too much, the electrons can accelerate. This process is referred to as self-trapping, but there are many other methods to inject electrons into the plasma bubble, usually with better control over the process. One example of this is to decrease the phase velocity of the plasma wave, forcing it to break. This can be achieved with some gas density

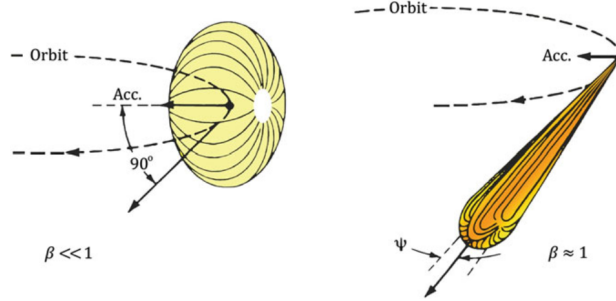


Figure 2.3: When non-relativistic particles undergo acceleration the shape of the electromagnetic radiation becomes that of a donut (left). Relativistic particles under acceleration radiate in the shape of a cone (right), directed perpendicular to the acceleration with an opening angle of  $2\Psi \approx \frac{2}{\gamma}$ .  $\beta$  is the ratio of the particles speed in relation the the speed of light,  $\beta = v/c$  [8].

modulation along the propagation axis [2].

The plasma bubble also exerts a focusing force on the electrons and due to the symmetry, an electron that sits on a central line in the bubble will remain roughly at this position as the focusing forces are about equal. In most cases however, the electrons are slightly off axis, forcing them to oscillate about the central axis instead and like any charged particle they will emit radiation as they undergo acceleration which is in many ways similar to a wiggler [6].

### 2.1.1 X-ray generation

When a charged particle is accelerated it emits radiation. The shape of the electromagnetic radiation is that of a dipole at non-relativistic speeds and is rotational symmetric, creating a 3-dimensional "donut" shape as shown in figure 2.3. When the particle speed increases and approaches the speed of light,  $c$ , the shape changes due to relativistic effects and becomes a narrow cone as shown in figure 2.3 with an opening angle of  $2/\gamma$ , where  $\gamma$  is the Lorentz factor [8].

This cone shaped radiation comes from the relativistic effect of time dilation. Consider a particle moving at a speed  $v$  that emits light perpendicular to its path. The emitted light will travel a distance  $c\Delta t_0$  during the time  $\Delta t_0$ , in the frame of the particle. As the path of the electron and the emitted light is perpendicular, no Lorentz contraction applies, so the perpendicular distance is the same in the electrons frame of reference as in the laboratory frame. The total light path in the laboratory frame is much longer however. As the speed of light is the same in both frames of reference the time intervals must be different. The light path length measured in the laboratory frame is thus, due to Pythagoras' theorem [9]

$$(c\Delta t)^2 = (c\Delta t_0)^2 + (v\Delta t)^2. \quad (2.5)$$



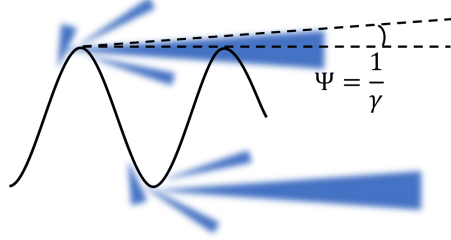


Figure 2.4: A particle following the sinusoidal path will emit radiation (depicted as blue cones) when it accelerates. As the largest acceleration is where the oscillations amplitude is largest, most of the radiation will be directed forward.

This implies that the direction of the light and particle path will approach each other as  $v$  approaches  $c$ . The angle between the emitted light and the path of the electron is

$$\Psi \approx \sin \Psi = \frac{\Delta t_0}{\Delta t} \quad (2.6)$$

Solving for  $\Delta t$  we have

$$\Delta t^2 = \frac{(c\Delta t_0)^2 + (v\Delta t)^2}{c^2} = \Delta t_0^2 + \frac{v^2}{c^2}\Delta t^2 \quad (2.7)$$

$$\Delta t = \frac{\Delta t_0}{\sqrt{1 - \frac{v^2}{c^2}}} = \gamma \Delta t_0 \quad (2.8)$$

where  $\gamma$  is the Lorentz factor, also called the relativistic factor. Inserting this again in equation 2.6, we have that the angle between the electron path and the light radiated is

$$\Psi \approx \frac{1}{\gamma}. \quad (2.9)$$

This means that due to the oscillatory motion of the electrons inside the plasma bubble, the radiated light is highly directed [6], this is illustrated in figure 2.4.

Due to the small scale of the system the apparent source is also very small. As the electrons oscillate they will produce a source size of a few micrometers and the wavelength of the oscillations is about 100  $\mu\text{m}$ . The electron bunch is also very short and this results in very short pulse duration of the produced x-rays. Its peak brightness has also been reported to be comparable to that of third generation light sources, making the compactness of the system appealing [6].

Further, it can be shown that the emitted spectrum is synchrotron-like and is described by [6]

$$\frac{d^2 I}{d\omega d\Omega} \simeq N_\beta \frac{3e^2}{2\pi^3 \epsilon_0 c^3} \frac{\gamma_{z0}^2 \zeta^2}{1 + \gamma_{z0}^2 \theta^2} \left[ \frac{\gamma_{z0}^2 \theta^2}{1 + \gamma_{z0}^2 \theta^2} \mathcal{K}_{1/3}^2(\zeta) + \mathcal{K}_{2/3}^2(\zeta) \right] \quad (2.10)$$

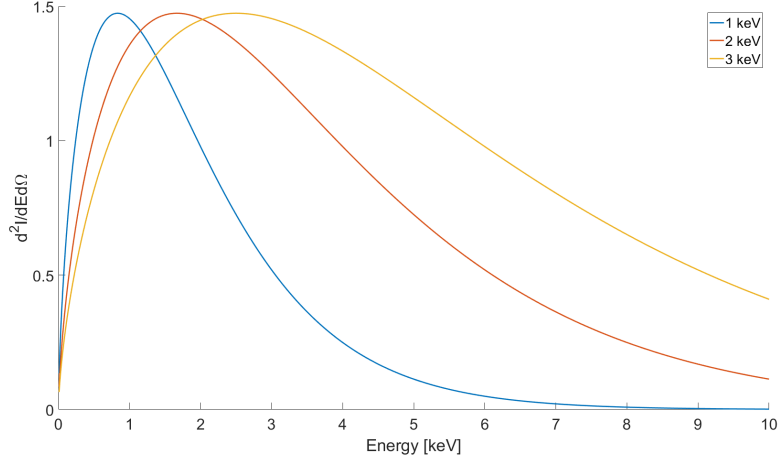


Figure 2.5: Normalized energy spectrum for critical energies 1 (blue), 2 (orange) and 3 (yellow) keV calculated by the use of equation 2.13

where

$$\zeta = \frac{E}{2E_c} (1 + \gamma_{z0}^2 \theta^2)^{3/2} \quad (2.11)$$

$$E_c = \frac{3}{2} \hbar \gamma_{z0}^3 \omega_\beta^2 r_\beta / c. \quad (2.12)$$

Here  $E_c$  is the critical energy of the spectrum,  $\omega_\beta = 2\pi/\sqrt{2\gamma}$ ,  $\gamma_{z0}$  is the initial relativistic factor and  $r_\beta$  describes the maximum amplitude of the electron oscillation. This can be simplified if one only looks at the radiation close to the optical axis, putting  $\theta = 0$  then gives

$$\frac{d^2 I}{(d\omega d\Omega)_{\theta=0}} \propto \gamma_{z0}^2 \xi^2 \mathcal{K}_{2/3}^2(\xi/2). \quad (2.13)$$

Here  $\xi = E/E_c$ ,  $\mathcal{K}_n$  is the modified Bessel function of order  $n$ ,  $N_\beta$  the number of electron oscillations,  $\theta$  the observation angle relative the propagation axis,  $z$ , and  $\gamma_{z0}$  is the initial Lorentz factor. Figure 2.5 shows the spectrum defined by equation 2.13 for different critical energies. A higher critical energy means that more high-energy photons are generated.

## 2.2 X-ray Propagation

This section is dedicated to the theory of diffraction. The method for source size determination used in this thesis is based solely on diffraction, hence it is an important topic in this thesis. There will also be a need to simulate some phase-contrast images before deciding on experimental parameters. Thus the

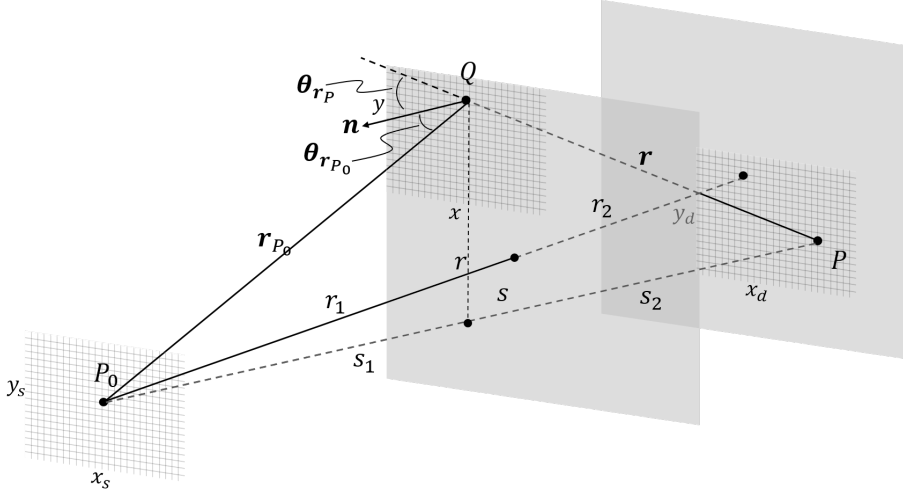


Figure 2.6: Showing the different vectors and distances used along with the 3 different coordinate systems  $(x_s, y_s)$ ,  $(x, y)$  and  $(x_d, y_d)$  for the source, aperture and detector respectively. The perpendicular distance between these coordinate systems are  $r_1$ ,  $r_2$  and  $r$ .  $\vec{n}$  is the unit normal to the aperture coordinate system

theory of diffraction and x-ray propagation is needed. This theory is general and applies to radiation of all wavelengths, but this thesis focuses on x-rays and as such, any wavelengths used are assumed to be in this range. The most general description is given by Kirchhoffs diffraction integrals which is presented in the following sections. These can, under the correct assumptions, be simplified to Fresnel diffraction which is explained later on.

### 2.2.1 Kirchhoff Diffraction

The solution to the wave equation at a point  $P$  can be formulated using Kirchhoff's diffraction formula. For a monochromatic point source at  $P_0$  with a wave field  $U_{P_0}$  with amplitude  $a$  it states that the wave field at  $P$  is [10]

$$\begin{aligned}
 U_P &= \frac{a}{4\pi} \int_S \frac{e^{-2\pi ikr}}{r} \cdot U_{P_0} \left[ \left( \frac{1}{r} + 2\pi ik \right) \cos(\theta_{rP}) - \left( \frac{1}{r_{P_0}} + 2\pi ik \right) \cos(\theta_{r_{P_0}}) \right] dS = \\
 &= \frac{a}{4\pi} \int_S \frac{e^{-2\pi ikr}}{r} \cdot \frac{e^{-2\pi ikr_{P_0}}}{r_{P_0}} \left[ \left( \frac{1}{r} + 2\pi ik \right) \cos(\theta_{rP}) - \left( \frac{1}{r_{P_0}} + 2\pi ik \right) \cos(\theta_{r_{P_0}}) \right] dS.
 \end{aligned} \tag{2.14}$$

Here,  $\theta_{rP}$  and  $\theta_{r_{P_0}}$  are the angles between the surface normal of the aperture to the vectors  $\vec{r}$  and  $\vec{r}_{P_0}$  with  $|\vec{r}| = r$  and  $|\vec{r}_{P_0}| = r_{P_0}$  illustrated in figure 2.6.  $k$  is the wavenumber  $k = 1/\lambda$ . The integration is done over the surface  $S$  of a sphere originating at  $P$  with radius  $r_{P_0}$ . Assuming that the distances are much

larger than the wavelength (which is usually the case) we can omit the terms  $\frac{1}{r_{P_0}}, \frac{1}{r}$  and are left with

$$U_P = \frac{ai}{2\lambda} \int \frac{e^{-2\pi ikr}}{r} \cdot \frac{e^{-2\pi kr_{P_0}}}{r_{P_0}} \left( \cos(\theta_{r_P}) - \cos(\theta_{r_{P_0}}) \right) dS. \quad (2.15)$$

This equation assumes propagation in free space and, without the presence of an object to perturb the wavefield, no diffraction of interest will be present.

One can introduce a transmission function,  $q(x, y)$  that represents the effect an object would have on the incident wave function. For example, an infinite perfect slit (that only varies in  $x$ ) would be represented by  $q(x) = |x| < w/2$  being unity inside this interval and 0 outside, where  $w$  is the width of the slit. Note that this transmission function is allowed to be complex, accounting for any phase change introduced by the object due to a change in refractive index. This transmission function would then be multiplied with equation 2.15, resulting in

$$U_P = \frac{ai}{2\lambda} \int \frac{e^{-2\pi ikr}}{r} \cdot \frac{e^{-2\pi kr_{P_0}}}{r_{P_0}} \left( \cos(\theta_{r_P}) - \cos(\theta_{r_{P_0}}) \right) q(x, y) dS. \quad (2.16)$$

Here it is assumed that the direction of propagation is  $z$ . This is well known and has been derived many times before, see for example "Diffraction physics" by J.M Cowley [10].

## 2.2.2 Fresnel Diffraction

If we assume that the distances  $r, r_{P_0}$  are much greater than the size of the aperture (the so-called small angle approximation) then, the aperture can be considered orthogonal to the direction of propagation and the cosine terms become approximately 1 and  $-1$ , resulting in

$$U_P = \frac{ai}{\lambda} \iint \frac{e^{-2\pi ik(r+r_{P_0})}}{r \cdot r_{P_0}} \cdot q(x, y) dx dy. \quad (2.17)$$

If we assume that the aperture lies in the coordinate system of  $(x, y, z)$ , the source in  $(x_s, y_s, z_s)$  and an arbitrary point after propagation is described by  $(x_d, y_d, z_d)$ . We have that

$$r_{P_0}^2 = r_2^2 + (x - x_d)^2 + (y - y_d)^2 \approx r_2 + \frac{(x - x_d)^2 + (y - y_d)^2}{2r_2}$$

where  $r_2$  is the perpendicular distance between the aperture and the detector plane. This is what is generally called the *Fresnel approximation*.

The wave at a distance  $r_2$  is then given by

$$U_P = \frac{ia}{r_2\lambda} e^{-2\pi ikr_2} \iint e^{\frac{-2\pi i\{(x-x_d)^2+(y-y_d)^2\}}{r_2\lambda}} q(x, y) dx dy. \quad (2.18)$$

This is known as Fresnel diffraction and was derived following "Diffraction physics" by J.M Cowley [10], a more in-depth derivation can be found there.

An effect of the diffraction is that the intensity is strongly modulated at edges, producing fringes, with the largest fringe closest to the edge. This is true even if the object is transparent, as it is the superposition of the perturbed wave and unperturbed wave that produces the intensity modulation. That means that as long as there is a difference in refractive index, this effect will be present. This is generally referred to as *edge enhancement* as this intensity modulation is strong at the boundary of a change in refractive index, making edges more visible [11]. Using this intensity modulation one can calculate backwards to find the wave functions phase (phase retrieval) and thereby calculate the spatial distribution of the refractive index in the object. The edge enhancement is in itself useful however in the case that edges are of interest and can be combined with absorption images for improved contrast.

### 2.2.3 Source Size Determination

The wave field a distance  $r$  from the source located at  $(x_s, y_s)$  that is disturbed by an object located at  $(x, y)$  a distance  $r_1$  with a finite transmission function can be written as [12], [13]

$$U(x_d, y_d) = U_0(x_d, y_d)(1 + g(x_d, y_d)). \quad (2.19)$$

where  $g(x_d, y_d)$  contains the terms that represents the disturbances imparted by the object and  $U_0(x_d, y_d)$  is the unperturbed wave field. This can be seen as a superposition of the original wave field and the perturbed one.

Using equation 2.16, the equation for Kirchhoff diffraction and rewriting it [12]

$$g(x_d, y_d) = -\frac{i}{2\lambda} e^{\frac{-i2\pi s}{\lambda}} \iint_A e^{\frac{i2\pi(s_1+s_2)}{\lambda}} \cdot \frac{1}{s_2 s_1} \left( \frac{r_2}{s_2} + \frac{r_1}{s_1} \right) \quad (2.20)$$

and by making the paraxial approximation again the integral can be rewritten to [12], [13]

$$g(x_d, y_d) = \iint \frac{M}{i\lambda r_2} \exp \left( i\pi/\lambda \left[ -\frac{(x_d - x_s)^2}{r_1 + r_2} - \frac{(y_d - y_s)^2}{r_1 + r_2} + \frac{(x - x_s)^2}{r_1} + \frac{(y - y_s)^2}{r_1} + \frac{(x - x_d)^2}{r_2} + \frac{(y - y_d)^2}{r_2} \right] \right) \cdot q(x, y) dx dy \quad (2.21)$$

where  $M = \frac{r_1+r_2}{r_1}$  is the magnification. If we assume the point source to be located at  $(x_s, y_s) = (0, 0)$  and introduce  $r = r_1 + r_2$  we have

$$g(x_d, y_d) = \iint \frac{M}{i\lambda r_2} \exp \left( i\pi/\lambda \left[ -\frac{x_d^2}{r} - \frac{y_d^2}{r} + \frac{x^2}{r_1} + \frac{y^2}{r_1} + \frac{(x - x_d)^2}{r_2} + \frac{(y - y_d)^2}{r_2} \right] \right) \cdot q(x, y) dx dy. \quad (2.22)$$

Assuming that the aperture only varies in  $x$  we can integrate over  $y$ .

$$\int_{-\infty}^{\infty} \exp\left(i\pi/\lambda\left[-\frac{y_d^2}{r} + \frac{y^2}{r_1} + \frac{(y-y_d)^2}{r_2}\right]\right) dy = \sqrt{\frac{\lambda r_1 r_2}{ir}} \cdot \exp\left(\frac{i\pi}{\lambda}\left[y_d^2\left(\frac{1}{r_2} + \frac{1}{r}\right) - \frac{2y_d}{4r_2\left(\frac{1}{r_2} + \frac{1}{r_1}\right)}\right]\right) dx \quad (2.23)$$

If we stay on the optical axis and only look at the intensity at  $y_d = 0$  we can ignore the extra phase term, we then have

$$g(x_d) = \int \sqrt{\frac{r}{i\lambda r_1 r_2}} \exp\left(i\pi/\lambda\left[-\frac{x_d^2}{r} + \frac{x^2}{r_1} + \frac{(x-x_d)^2}{r_2}\right]\right) \cdot q(x) dx. \quad (2.24)$$

Rearranging this equation to

$$g(x_d) = \int \sqrt{\frac{r}{i\lambda r_1 r_2}} \exp\left(\frac{i\pi}{\lambda r_2}\left[x_d^2 \frac{r_1}{r} + x^2 \frac{r}{r_1} - 2x \cdot x_d\right]\right) \cdot q(x) dx, \quad (2.25)$$

then normalized intensity (with respect to  $E_0(x_d, y_d)$ ) becomes [13]

$$I = 1 + g + g^* + |g|^2 = 1 + |g|^2 \quad (2.26)$$

as  $g^* = -g$  since  $\Re(g) = 0$ , and as we are only interested in the interference pattern we can subtract the reference field and are left with  $|g|^2$ , i.e

$$I(x_d) = \left| \sqrt{\frac{r}{i\lambda r_1 r_2}} \int \exp\left(\frac{-i\pi}{\lambda r_2}\left(2xx_d - \frac{r}{r_1}x^2 - \frac{r_1}{r}x_d^2\right)\right) \cdot q(x) dx \right|^2. \quad (2.27)$$

This same equation can be found in the article by I. N. Tilikin *et al.* [14] and the following derivation is guided by this report. The simplest aperture for a source size measurement is probably that of a wire as there is no issue of alignment. A wire is very thin at the edges compared to its center and will be more transparent here, this can be taken into account using Beer-Lamberts law that describes the intensity after passing through a homogeneous object as

$$I = I_0 e^{-\mu \cdot l} \quad (2.28)$$

where  $\mu$  is the linear attenuation coefficient,  $I_0$  the incident intensity and  $l$  the distance traveled through the material. For a wire, the propagation distance is  $2\sqrt{R^2 - x^2}$  which can easily be shown using Pythagoras theorem, where  $R$  is the radius of the wire.

The attenuation coefficient is dependent on the wavelength of the radiation so unless the beam is monochromatic this has to be taken into account. We then have the intensity after a wire of radius  $R$  as

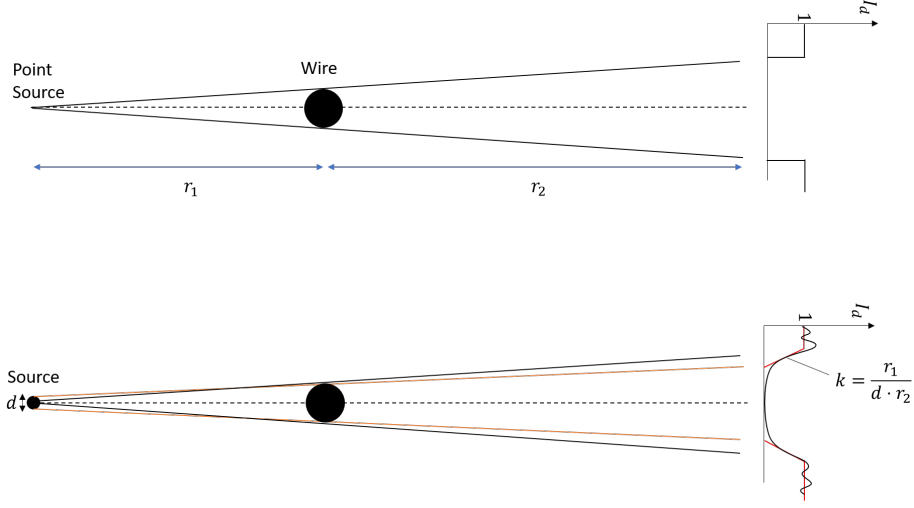


Figure 2.7: A point source would give a very sharp shadow and due to an extended source size, each point can be thought of as a point source, interfering with the others, giving rise to a diffraction pattern. The linear approximation of the slope  $k$ , shown in red, of the diffraction pattern is  $\frac{r_1}{d \cdot r_2}$  and thus depends on the source size [14].

$$I = I_0 e^{-\mu(\lambda) \cdot 2\sqrt{R^2 - x^2}} \quad (2.29)$$

where  $\mu$  is the linear attenuation coefficient of the material.

The x-ray detector's quantum efficiency also needs to be taken into account. The quantum efficiency tells how many of the photons of a certain energy that hit the detector is actually detected. Therefore we multiply the intensity with the quantum efficiency.

This wavelength dependency adds another dimension to the problem. By taking into account both the quantum efficiency of the detector and the attenuation one can take the weighted average as

$$\bar{I}(x_d) = \frac{\int I(x_d, \lambda) w(\lambda) Q(\lambda) d\lambda}{\int w(\lambda) d\lambda} \quad (2.30)$$

where  $w(\lambda)$  are the weights determined by the spectrum in 2.13 and  $Q(\lambda)$  is the quantum efficiency. This takes into account the shape of the energy spectrum.

Equation 2.27 refers to a point source, but if the source is extended the diffraction pattern will be smeared as each point in the source gives the same pattern as the others, but it is shifted by  $x_s \frac{r_2}{r_1}$  [14], where  $x_s$  is the transverse coordinate for the source, see figure 2.7. If we assume the source to have a Gaussian distribution as

$$B(x_s) = \frac{e^{-\frac{x_s^2}{2\sigma^2}}}{\sigma\sqrt{2\pi}} \quad (2.31)$$

we have that, for a source size  $d$  (FWHM), the standard deviation of  $B(x_s)$  is  $\sigma = \frac{d}{2\sqrt{2\ln 2}}$ .

This means that the intensity needs to be integrated over all the points in the source, each shifted by  $x_s \frac{r_2}{r_1}$ . Thus, we have [14]

$$I_s(x_d) = \int B(x_s) \bar{I}(x_d + x_s \frac{r_2}{r_1}) dx_s \quad (2.32)$$

and equation 2.32 will, for a given source size, give the corresponding diffraction pattern from an object described by  $q(x)$ . By simulating this for many different source sizes and fitting the experimental data one can then determine the source size with a simple measurement that only requires an aperture that varies in  $x$ , such as a slit, edge or a wire.

## 2.3 Phase Contrast

The concept of phase-contrast imaging was realized for the first by Frits Zernike in 1953. This was an important improvement to the techniques at the time as it removed the necessity to use chemical agents in biological microscopy and greatly enhancing the contrast, especially in biological samples which have very little absorption. This, along with the development of the phase-contrast microscope did, in the end, earn him a Nobel prize [15].

The basic idea of phase-contrast imaging is to use the information contained in the phase of the light as it has interacted with an object. The refractive index,  $n = 1 - \delta + i\beta$ , where  $\delta$  represents the change in phase and  $\beta$  the absorption, is the desired quantity. Conventional radiography uses the absorption which is easily detected in the intensity, but for phase-contrast imaging the change in phase the electromagnetic wave undergoes is not directly measurable. Instead one measures the intensity modulation created by the phase change and from this, the phase can be calculated. This process is generally referred to as phase retrieval and once this is calculated, the objects projected thickness may also be obtained.

When a tomographic reconstruction is desired one needs a connection between the detected intensity and the thickness of the sample. This is directly given by an absorption image as the intensity decreases for thicker objects in accordance with Beer-Lambert's law. It is however less prominent when the sample absorbs very little in comparison to the surrounding material. Phase-contrast imaging on the other hand is more sensitive to a change in the refractive index, as will be shown later, and can therefore give much better contrast for these samples. This makes the technique very useful for thin samples as they have very little absorption, and also biological samples as the difference in ab-



sorption between an area of interest and its surroundings can be very small, for example a tumor surrounded by healthy tissue.

To use phase-contrast images for tomography one needs to have a connection between the detected intensity and the thickness of the sample and this is less straightforward than in the case of absorption tomography. Unfortunately, the technique developed by Zernike is not well suited for X-ray imaging as it relies heavily on optics. There are however a number of other techniques developed for this regime [16]. To mention a few of these, there are grating based (Talbot interferometer), crystal interferometer, prism interferometer, analyzer-based imaging, and propagation based imaging [17]. All of these methods, except one, use some sort of optics, be it a grating or a crystal. Propagation based, also known as *in-line* phase-contrast imaging, uses no optical elements and from an experimental point of view this is by far the simplest technique. The drawback of this method however is that it is harder to retrieve the phase from the intensity images compared to other methods and the phase retrieval algorithms are thus more complex [18].

### 2.3.1 In-line Phase Contrast

For the remainder of this thesis, the method focused on will be in-line phase contrast, also known as propagation based phase contrast.

This method requires a way to obtain the phase, so called *phase retrieval*, and there are several ways to do this. They are all similar in the sense that they all give a relation between measured intensity and phase. The most obvious and straight-forward way to do this is to take two intensity measurements. The first measurement is taken with the detector very close to the sample. In this region the detected intensity will mainly give information about the absorption as the phase variations have not yet had time to develop enough to give rise to an intensity modulation. Then, a second intensity measurement is taken with the detector further away. This measurement will be dominated by the intensity modulation due to the change in phase, and since the absorption is known from the first measurement, this gives full knowledge of the phase. It is however difficult and inconvenient to take two measurements under the same conditions and if one makes some assumption of the sample this can be avoided [18].

In the work by A.Burvall *et al.* [18] an overview and comparison is given between different phase retrieval methods that use only a single measurement. Figure 2.1 gives an overview for different methods available and the difference between them. Figure 2.8 shows a flow chart on how to choose a phase-retrieval method based on the results gathered by A.Burvall *et al* [18]. Following this procedure for the experimental setup, see section 3.2, one comes to the conclusion that either the Single material or the modified Bronnikov should be used for this setup (see section 3). Both perform similarly [18] but the modified Bronnikov is somewhat more cumbersome to implement as there exists a correction factor  $\alpha$  that is found using a semi-empirical approach, comparing simulations and experiment [19]. The Single material algorithm is more straight forward and as such, the choice comes down to the use of Paganinis Single Material algorithm.

Method	$\mu \approx 0$	$\mu \propto \delta$	$\frac{a^2}{r_2 \lambda} \gg 1$	SVP	Born	Rytov
Bronnikov	✓		✓			
Modified Bronnikov	✓		✓			
Phase-att. duality		✓	✓	✓		
Single material		✓	✓			
Two materials			✓	✓		
Fourier (Born) a		✓			✓	
b	✓					
Fourier (Rytov) a		✓				✓
b	✓					

Table 2.1: A quick overview and comparison of different phase retrieval methods. Bronnikov assumes that the absorption in the sample is very low, phase-attenuation duality assumes that the absorption  $\mu$  and the decrement in refractive index  $\delta$  is known. The same is true for the Single material method. All methods except Fourier methods assume the Fresnel number to be much larger than 1. Two methods assume the slowly varying phase approximation (SVP), i.e. phase-attenuation duality and Two materials. The Fourier methods come in two flavors, one that uses the Born approximation and one that uses the Rytov approximation [18].

### 2.3.2 Single material Phase Retrieval

As with many things, this starts at the simple statement that energy must be conserved, which translates to the divergence of the Poynting vector,  $\vec{S}$ , being zero [20].

$$\nabla \cdot \vec{S}(\vec{r}) = 0 \quad (2.33)$$

In the case of a coherent wave this may be written as [20]

$$\nabla \cdot (I(\vec{r}) \nabla \phi(\vec{r})) = 0 \quad (2.34)$$

where  $I$  is the intensity and  $\phi$  the phase of the wave. By making the paraxial approximation we arrive at [21]

$$\nabla_{\perp} \cdot (I(\vec{r}_{\perp}, z) \nabla_{\perp} \phi(\vec{r}_{\perp}, z)) = -\frac{2\pi}{\lambda} \frac{\partial}{\partial z} I(\vec{r}_{\perp}, z). \quad (2.35)$$

where  $k = 2\pi/\lambda$  is the wave number,  $\nabla_{\perp}$  and  $r_{\perp}$  is the gradient operator and position vector in the plane of  $(x, y)$  and  $z$  denotes the optical axis. This was shown by Teauge [1983], Rytov *et al.* [1989] and is called the Transport of Intensity equation (TIE). This describes the change in intensity as a paraxial monochromatic wave propagates. Note that due to the paraxial approximation, we assume a point source and a magnification,  $M$ , close to 1.

The object of interest is assumed to be of a single known material and is thus also assumed to follow Beer-Lambert's law of absorption, equation 2.28, with  $l = T(\vec{r}_{\perp})$  that corresponds to the projected thickness.

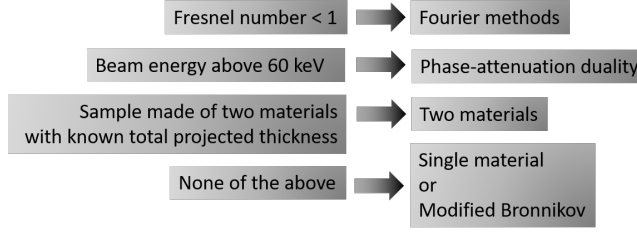


Figure 2.8: This flowchart is based on the results in “Phase retrieval in x-ray phase-contrast imaging suitable for tomography by A.Burvall *et al.* [18] and allows for a quick way to choose your method of phase retrieval once you know your sample and experimental setup.

Further, if the object is thin enough it follows that the phase of the wavefront when it leaves the objects surface is proportional to the projected thickness  $T(\vec{r}_\perp)$  and the phase-change factor of the index of refraction  $\delta$  [21].

$$\phi(\vec{r}_\perp, z = 0) = -\frac{2\pi}{\lambda}\delta T(\vec{r}_\perp) \quad (2.36)$$

By substituting these two equations (2.28, 2.36) into the transport of intensity equation, 2.35 we arrive at

$$\delta \nabla_\perp \cdot (I_{in} e^{-\mu T(\vec{r}_\perp)} \nabla_\perp T(\vec{r}_\perp)) = \frac{\partial}{\partial z} I_{in} e^{-\mu T(\vec{r}_\perp)} \quad (2.37)$$

where we have the relation

$$\mu = \frac{4\pi}{\lambda}\beta = 2k\beta.$$

By making use of

$$\delta \nabla_\perp \cdot (e^{-\mu T(\vec{r}_\perp)} \nabla_\perp T(\vec{r}_\perp)) = -\frac{\delta}{\mu} \nabla_\perp^2 e^{-\mu T(\vec{r}_\perp)}$$

it further simplifies to

$$-\frac{\delta}{\mu} I_{in} \nabla_\perp^2 e^{-\mu T(\vec{r}_\perp)} = \frac{\partial}{\partial z} I(\vec{r}_\perp, z = 0). \quad (2.38)$$

Approximating the right hand side of this equation using a finite difference, i.e

$$\frac{\partial}{\partial z} I(\vec{r}_\perp, z = 0) \approx \frac{I(\vec{r}_\perp, z = r_2) - I_{in} e^{-\mu T(\vec{r}_\perp)}}{r_2} \quad (2.39)$$

where  $r_2$  is the object-detector distance. We then have

$$-\frac{\delta}{\mu} I_{in} \nabla_\perp^2 e^{-\mu T(\vec{r}_\perp)} = \frac{I(\vec{r}_\perp, z = r_2) - I_{in} e^{-\mu T(\vec{r}_\perp)}}{r_2}. \quad (2.40)$$

Rearranging this to

$$\left(\frac{r_2\delta}{\mu}\nabla_{\perp}^2 + 1\right)I_{in}e^{-\mu T(\vec{r}_{\perp})} = I(\vec{r}_{\perp}, z = r_2) \quad (2.41)$$

and rewriting equation 2.41 with the Fourier integrals

$$I_{in}e^{-\mu T(\vec{r}_{\perp})} = \frac{I_{in}}{2\pi} \iint \mathcal{F}(e^{-\mu T(\vec{r}_{\perp})})e^{i\vec{k}_{\perp}\cdot\vec{r}_{\perp}}d\vec{k}_{\perp}$$

$$I(\vec{r}_{\perp}, z = r_2) = \frac{1}{2\pi} \iint \mathcal{F}(I(\vec{r}_{\perp}, z = r_2))e^{i\vec{k}_{\perp}\cdot\vec{r}_{\perp}}d\vec{k}_{\perp}$$

we have

$$\mathcal{F}(e^{-\mu T(\vec{r}_{\perp})}) = \mu \frac{\mathcal{F}(I(\vec{r}_{\perp}, z = r_2))/I_{in}}{r_2\delta|\vec{k}_{\perp}|^2 + \mu}. \quad (2.42)$$

Here,  $\vec{k}_{\perp}$  is the spatial frequency vector,  $\vec{k} = (u, v)$ , so that  $|\vec{k}_{\perp}| = u^2 + v^2$ . Taking the inverse Fourier transformation along with the natural logarithm we finally end up with an expression for the projected thickness

$$T(\vec{r}_{\perp}) = -\frac{1}{\mu} \ln \left( \mathcal{F}^{-1} \left( \mu \frac{\mathcal{F}(I(\vec{r}_{\perp}, z = r_2))/I_{in}}{r_2\delta|\vec{k}_{\perp}|^2 + \mu} \right) \right). \quad (2.43)$$

This corresponds to the projected thickness observed when illuminated by a point source. This was originally derived by Paganin [21] and the derivation above follows the original very closely. Using equation 2.43 the projected thickness of a sample can be calculated from the phase contrast images and these can be used to do a tomographic reconstruction.

Looking at the denominator one may suspect that it will also act as a 1-st order low-pass filter in the frequency domain in the form of

$$I_{out}/I_{in} = \frac{1}{|\vec{k}_{\perp}|^2\alpha + 1} \quad (2.44)$$

where  $K$  would be the gain and  $\alpha$  the inverse cut-of frequency, causing images to be slightly blurred and loosing some of the finer details.

Since the source is not a point source however, one needs to take into account the magnification  $M$ . Paganin *et al.* mentions one way of doing this [21] but this thesis takes a different approach.

To fully calculate 2.43 one needs to first transfer the spatial coordinates into spatial frequencies,  $\vec{k}_{\perp}$ . If the number of pixels for the detector is  $n_x, n_y$  and size of each pixel is  $d_x, d_y$ . Then the number of pixels per unit length (u.l) is

$$\begin{cases} Fs_x = \frac{1}{d_x} \\ Fs_y = \frac{1}{d_y} \end{cases}$$

and the number of possible cycles per u.l is

$$\begin{cases} dF_x = \frac{Fs_x}{n_x} \\ dF_y = \frac{Fs_y}{n_y} \end{cases}$$

where  $dF_x \cdot dF_y$  is the inverse of the detector area. This means that the smallest spatial frequency (that is detectable) has a wavelength that is as long as the detector, (as a long wavelength corresponds to a low frequency). Note that the wavelength in this case refers to a periodic intensity modulation on the detector. This means that in the spatial frequency grid we want the size of each grid point, i.e.  $dF_x, dF_y$ , to be of a size that allow us to detect as low frequencies as possible. The highest spatial frequency on the other hand would correspond to the shortest wavelength detectable. The smallest one would be a wavelength that covers 2 pixels (otherwise one can not know that it has repeated itself). This means that the highest spatial frequency one can detect is

$$\frac{Fs_x}{2} = \frac{1}{2d_x}$$

which one might recognize as Nyquist's sampling theorem.

Thus, the spatial frequency grid would be

$$\begin{aligned} & \left\{ \frac{Fs_x}{2}, \frac{Fs_x}{2} + dF_x, \dots, \frac{Fs_x}{2} + (n_x - 1) \cdot dF_x \right\} \\ & \left\{ \frac{Fs_y}{2}, \frac{Fs_y}{2} + dF_y, \dots, \frac{Fs_y}{2} + (n_y - 1) \cdot dF_y \right\}. \end{aligned}$$

The spatial frequencies of interest are those in the object-plane however and since some magnification is present, this is not the same at the detector-plane. By dividing the pixel size by the magnification,  $M$ , this would correspond to the spatial frequencies in the object plane, resulting in a spatial frequency grid of

$$\begin{aligned} \vec{k}_x &= \left\{ \frac{-M \cdot Fs_x}{2}, \frac{-M \cdot Fs_x}{2} + dF_x, \dots, \frac{M \cdot Fs_x}{2} + (n_x - 1) \cdot dF_x \right\} \\ \vec{k}_y &= \left\{ \frac{-M \cdot Fs_y}{2}, \frac{-M \cdot Fs_y}{2} + dF_y, \dots, \frac{M \cdot Fs_y}{2} + (n_y - 1) \cdot dF_y \right\}. \end{aligned}$$

## 2.4 Tomography

The following section is dedicated to deriving the Radon transform along with its inverse and is closely following the derivation in T.M.Buzug, "Two-Dimensional Fourier-Based Reconstruction Methods" [22]. The Radon transform creates a series of projections over 180 degrees of an object and the inverse Radon transform does the opposite. It reconstructs the object from a series of projection images taken over 180 degrees. As the intention is to calculate the projected thickness from the phase contrast images, the inverse radon transform can be done on this set of images, taken over 180 degrees and reconstruct the object.

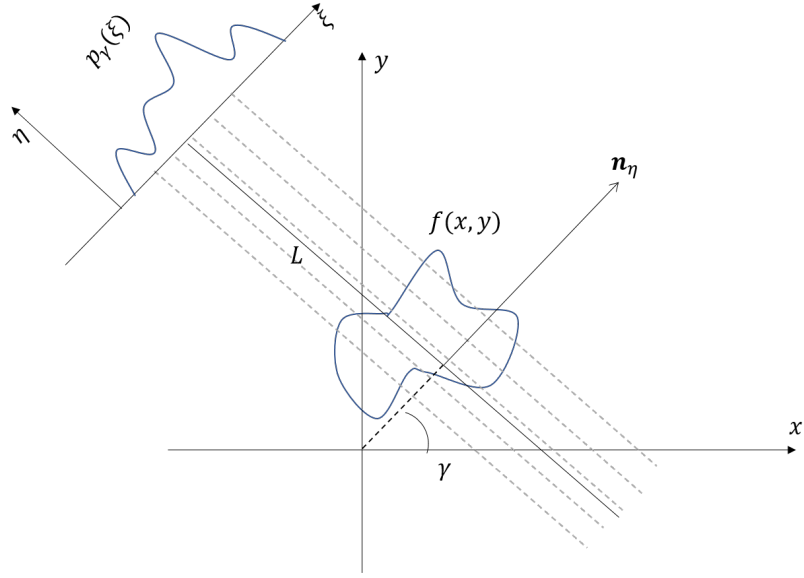


Figure 2.9: An illustration of the 2D Radon transform,  $p_\gamma(\xi)$ . It relates the line integrals parallel to the line  $L$ , which in turn is described by the angle  $\gamma$  defined by the angle between  $\xi$  and  $x$ . The object is described by the function  $f(x, y)$ .

### 2.4.1 Radon Transformation

Lets first define the projection integral as

$$p(s) = \int_0^s \mu(\eta) d\eta. \quad (2.45)$$

Here,  $\mu$  is the linear attenuation coefficient,  $\eta$  is a line that all x-rays are parallel to. Figure 2.9 shows how the coordinate system is set up. Parallel X-rays are incident on the object  $f(x, y)$  along the line  $L$ , that is parallel to  $\eta$ . The angle between the projection plane  $(\xi, \eta)$  and the object plane  $(x, y)$  is  $\gamma$  and this can be changed by either rotating the source around the object or rotating the object. The relation between the two coordinate systems is therefore

$$\xi = x \cdot \cos \gamma + y \cdot \sin \gamma = \vec{r}^T \cdot \vec{n}_\xi \quad (2.46)$$

$$\eta = -x \cdot \sin \gamma + y \cdot \cos \gamma = \vec{r}^T \cdot \vec{n}_\eta \quad (2.47)$$

where  $\vec{n}_\eta, \vec{n}_\xi$  are the unit vectors in  $(\eta, \xi)$ ,  $\vec{r} = (x, y)^T$  and  $(\cdot)^T$  denotes the transpose.

Expressing  $\mu$ , the linear attenuation coefficient in equation 2.45, we have

$$f(x, y) = \mu(\xi(x, y), \eta(x, y)) = \mu((\vec{r}^T \cdot \vec{n}_\xi), (\vec{r}^T \cdot \vec{n}_\eta)). \quad (2.48)$$

The projection integral only takes the projection along a single line, as there are multiple x-rays the full projection is given by the convolution

$$f * \delta(\vec{L}) = \int_{\mathcal{R}^2} f(\vec{r}) \delta(\vec{r} - \vec{L}) d\vec{r}. \quad (2.49)$$

Here the convolution is denoted by  $*$  and  $\delta$  is the Dirac function. Substituting  $L$  for  $\xi$  and using the fact that  $\vec{r} = x \cos \gamma + y \sin \gamma$  we have

$$f * \delta(\vec{L}) = \iint f(x, y) \delta(x \cos \gamma + y \sin \gamma - \xi) dx dy = p_\gamma(\xi) \quad (2.50)$$

where  $p_\gamma(\xi)$  is called the Radon transform and projects a function onto  $\xi$  over the angles  $\gamma$ . This transformation produces an image of sinusoidal patterns and is therefore also referred to as a sinogram. Note that this only contains information for a plane in  $(x, y, M)$  with  $z = M$ .

## 2.4.2 Inverse Radon Transformation

The Radon transform, equation 2.50, produces a set of projection images of an object but in X-ray imaging it is usually the other way around. One already has the projection images and wishes to know about the spatial distribution of the attenuation values of an object. That means that the *Inverse Radon Transform* is more interesting.

An important theorem makes the inverse Radon transform possible, the *Fourier slice theorem*, also called *Central slice theorem* and can be stated as "The Fourier transform of a parallel projection of an object  $f(x, y)$  obtained at angle  $\gamma$  equals a line in a 2D Fourier transform of  $f(x, y)$  taken at the same angle [23].

The Fourier transform of the projection data  $p_\gamma(\xi)$  is

$$P_\gamma(q) = \int_{-\infty}^{\infty} p_\gamma(\xi) e^{-2\pi i q \xi} d\xi \quad (2.51)$$

and the Fourier transform of the original function  $f(x, y)$  is

$$F(u, v) = \mathcal{F}(f(x, y)). \quad (2.52)$$

Here, a change of coordinates is needed as the projection data is in polar coordinates and the goal is to find  $f(x, y)$ . The Fourier transform does not change the nature of the coordinate system and the change can be carried out. Thus, changing from the frequency space of projections to the frequency space of the object we have a change of coordinates as

$$\begin{aligned} u &= q \cos \gamma \\ v &= q \sin \gamma \end{aligned} \quad (2.53)$$

Thus, we have

$$F(u, v) = F(q \cos \gamma, q \sin \gamma) = F(q, \gamma) \quad (2.54)$$

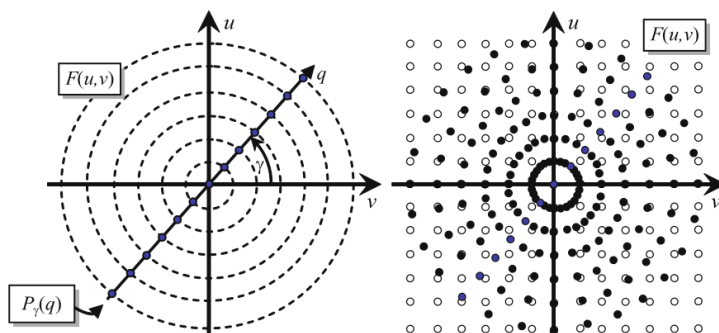


Figure 2.10: The equidistantly spaced values of  $q$  in the polar configuration (left), obtained from the projection data, needs to be interpolated as they only coincide with the Cartesian  $u, v$  on the axis (right). The grid density also changes, making interpolation errors more prominent at higher frequencies [22].

and thanks to the Fourier slice theorem we know that  $F(q, \gamma) = P_\gamma(q)$ , therefore we have

$$F(u, v) = P_\gamma(q) \quad (2.55)$$

where we have

$$P_\gamma(q) = \int_{-\infty}^{\infty} p_\gamma(\xi) e^{-2\pi i q \xi} d\xi = \int_{-\infty}^{\infty} \left( \int \mu(\xi, \eta) d\eta \right) e^{-2\pi i q \xi} d\xi. \quad (2.56)$$

So if the sinograms/projection data is known, i.e  $p_\gamma(\xi)$ , one simply has to take the 1-dimensional Fourier transform of this, then take the 2-dimensional inverse Fourier transform to obtain  $f(x, y)$ .

Despite the seemingly simple reconstruction formula there are other difficulties. The projection data, the data that is measured, lies in a polar coordinate system. One can think of it as a grid of concentric circles with increasing radii. This polar coordinate system needs to be "regridded" as the 2 dimensional Fourier transform lies in a square grid of  $u, v$  and needs appropriate interpolation. Figure 2.10 shows an illustration of this and the grid points only exactly coincide on the cartesian axis  $u, v$  in the frequency plane. As the grid density also changes, becoming sparser for higher frequencies, the interpolation error increases here, making it very sensitive to noise and at the same time resolving details in the image with lower accuracy.

There are several methods to deal with this problem, such as the linogram method, but this will not be covered in this thesis, see for example "computed tomography" by T.T Buzug [22] for more details.

### 2.4.3 Filtered backprojection

Instead of the direct inversion method mentioned above, the method used in most applications is the filtered backprojection.



Starting with the inverse Fourier transform of  $F(u, v)$  we have

$$f(x, y) = \iint F(u, v) e^{2\pi i(xu + yv)} du dv. \quad (2.57)$$

Expressing this in the polar coordinates of  $q, \gamma$  with the relation in equation 2.53 and with the Jacobian

$$J = \left| \begin{array}{cc} \frac{\partial u}{\partial q} & \frac{\partial v}{\partial q} \\ \frac{\partial u}{\partial \gamma} & \frac{\partial v}{\partial \gamma} \end{array} \right| = q(\cos^2 \gamma + \sin^2 \gamma) = q \quad (2.58)$$

we have

$$f(x, y) = \int_0^{2\pi} \int_0^\infty F(q \cos \gamma, q \sin \gamma) e^{2\pi i q(x \cos \gamma, y \sin \gamma)} q dq d\gamma. \quad (2.59)$$

This integral can be split in the  $\gamma$  variable as

$$\begin{aligned} f(x, y) &= \int_0^\pi \int_0^\infty F(q \cos \gamma, q \sin \gamma) e^{2\pi i q(x \cos \gamma, y \sin \gamma)} q dq d\gamma \\ &+ \int_\pi^{2\pi} \int_0^\infty F(q \cos \gamma, q \sin \gamma) e^{2\pi i q(x \cos \gamma, y \sin \gamma)} q dq d\gamma \end{aligned} \quad (2.60)$$

and by changing the outer integration limits once again through the introduction of the phase shift of  $\pi$  to

$$\begin{aligned} f(x, y) &= \int_0^\pi \int_0^\infty F(q \cos \gamma, q \sin \gamma) e^{2\pi i q(x \cos \gamma, y \sin \gamma)} q dq d\gamma \\ &+ \int_0^\pi \int_0^\infty F(q \cos \gamma + \pi, q \sin \gamma + \pi) e^{2\pi i q(x \cos \gamma + \pi, y \sin \gamma + \pi)} q dq d\gamma. \end{aligned} \quad (2.61)$$

Due to the symmetric properties of the Fourier transform we have the relations of the real and imaginary parts as

$$\begin{aligned} \Re(F(q, \gamma)) &= \Re(F(-q, \gamma + \pi)) = \Re(F(-q, \gamma)) = \Re(F(q, \gamma + \pi)) \\ \Im(F(q, \gamma)) &= \Im(F(-q, \gamma + \pi)) = -\Im(F(-q, \gamma)) = -\Im(F(q, \gamma + \pi)). \end{aligned} \quad (2.62)$$

Using this symmetry we can substitute the phase shift of  $\pi$  by changing signs on  $q$ , nullifying the sign change in  $F(q, \gamma)$  by changing integration boundaries to

$$\begin{aligned} f(x, y) &= \int_0^\pi \int_0^\infty F(q \cos \gamma, q \sin \gamma) e^{2\pi i q(x \cos \gamma, y \sin \gamma)} q dq d\gamma \\ &+ \int_0^\pi \int_{-\infty}^0 F(q \cos \gamma, q \sin \gamma) e^{2\pi i q(x \cos \gamma, y \sin \gamma)} q d(-q) d\gamma. \end{aligned} \quad (2.63)$$

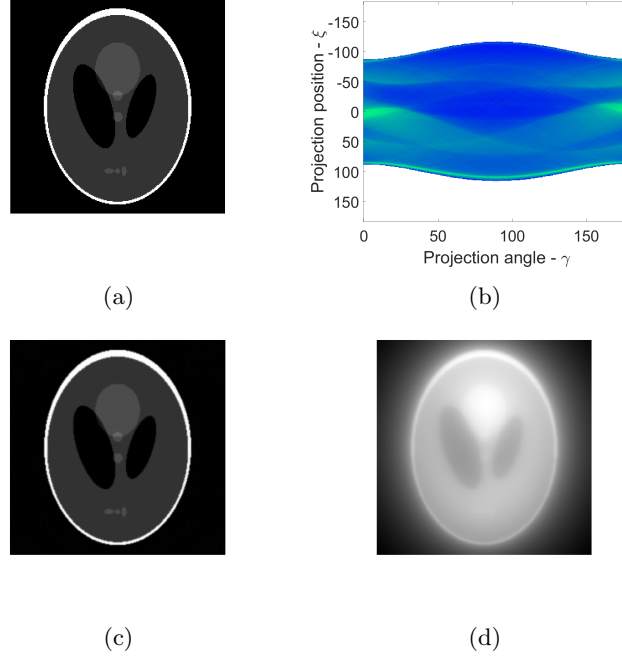


Figure 2.11: Illustration of the difference between filtered (c) and unfiltered (d) backprojection of a Shepp-Logan phantom (a). The sinogram used for reconstruction is also depicted in (b). The projections were simulated using MATLAB's standard functions for 179 angles with 1 degree increments on the  $256 \times 256$  image in a).

and rewriting this as a single term

$$f(x, y) = \int_0^\pi \int_{-\infty}^{\infty} F(q \cos \gamma, q \sin \gamma) e^{2\pi i q(x \cos \gamma, y \sin \gamma)} |q| dq d\gamma \quad (2.64)$$

and according to equation 2.55, together with the fact that  $\xi = x \cos \gamma + y \sin \gamma$ , we have

$$f(x, y) = \int_0^\pi \int_{-\infty}^{\infty} P_\gamma(q) e^{2\pi i q \xi} |q| dq d\gamma = \int_0^\pi h_\gamma(\xi) d\gamma \quad (2.65)$$

where  $h_\gamma(\xi)$  is the filtered projection, derived following [22]. Studying equation 2.65 reveals that it acts as a linear high-pass filter (ramp filter) for the projection data as it is weighted with  $q$ . Removing this factor, i.e.  $|q|$ , one would end up with  $p_\gamma(\xi)$ , the first form of the projection inversion derived. Equation 2.65 is the filtered backprojection and figure 2.11 shows the difference between unfiltered and filtered backprojection. These images were simulated using MATLAB and the built in Shepp-Logan phantom, which is a standard test image for tomography, meant to simulate a human head with regions of interest.

# Chapter 3

## Methodology

This section describes setup used for the source size measurement and the phase contrast imaging, some components more important to the experiments are explained more in detail. The general setup is the same in both cases and very similar to a standard LWFA experiment, with the difference of an x-ray CCD being present along with a sample holder. This section also describes the implementation of the algorithms used for various calculations, such as source size simulation, x-ray propagation simulation, projected thickness calculation, tomographic reconstruction and image alignment.

### 3.1 Lund Multi-TW Laser

The Lund multi-TW laser system is based on the chirped pulse (CPA) technique and figure 3.1 shows a schematic view of the setup. The gain medium in the system is titanium-doped sapphire and is pumped using frequency-doubled Nd:YAG lasers to a wavelength of 532 nm. The oscillator is based on Kerr lens mode-locking, resulting in an 80 MHz pulse train with a pulse duration of less than 30 fs. A Pockels cell pulse-picker reduces the repetition rate to 10 Hz before the first amplification stage. The multipass pre-amplifier increases the energy from 5 nJ to a few  $\mu\text{J}$ . A grating-based stretcher then chirps the pulse with a stretching ratio of 9 ps per nm bandwidth and the pulse duration is extended to about 450 ps. The pulses are then switched into an optical resonator using a Pockels cell, this is the regenerative amplifier. After 10-15 round trips in the resonator the pulse energy increases to a few mJ and the pulse is switched out again. The beam is expanded to a diameter of 8 mm and sent to a 5-pass amplifier where the energy increases to 400 mJ and pulses are temporally cleaned by two separate Pockels cells. Here the beam is split into two parts going to different experimental setups and the beam of interest is left with an energy of 150 mJ. The remainder is cleaned in a spatial filter, expanded to a diameter of 16 mm and amplified again in a 6-pass amplifier. This amplifier is pumped by 5 Nd:YAG lasers, resulting in a pulse energy of about 1.5-1.8 J. Finally, the

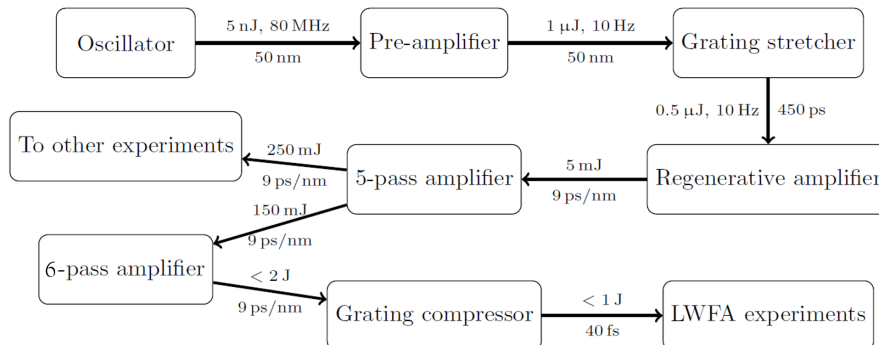


Figure 3.1: A schematic representation of the laser system [2].

beam enters a compression stage after being expanded to 60-65 mm and the result is a pulse duration down to 35 fs. The compression uses an acousto-optic programmable dispersive filter to compensate for higher-order spectral phase variations. From here on the beam propagates in vacuum to prevent filamentation and other nonlinear effects [2]. This system is evolving continuously, these parameters may very well change over time and this refers to the general setup used in the experiments done in this thesis.

## 3.2 Experimental Setup

As mentioned in the introduction, one advantage with in-line phase contrast compared to other techniques, such as grating based phase contrast, is that the setup is very simple. Figure 3.3 shows a schematic view of the experimental setup used for the tomography scans and figure 3.4 shows a photograph of the setup. The laser pulse enters a gas cell manufactured in aluminum where electrons are accelerated via wake-field acceleration. They enter a dispersive bending magnet and are detected by a CCD behind a scintillating screen while the x-ray beam continues toward the sample mounted in the sample holder. The figure is not according to scale and the x-ray CCD is further from the sample holder, at least 1.8 m. This setup or, very similar setups were used for all experiments. The main difference would be when measurements of the source size was carried out, the tungsten

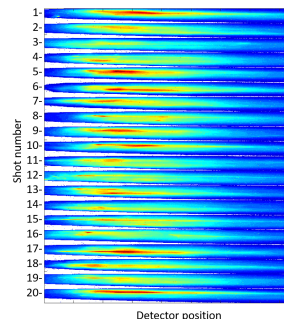


Figure 3.2: Dispersed electron beam for 20 consecutive shots recorded on a scintillating screen.

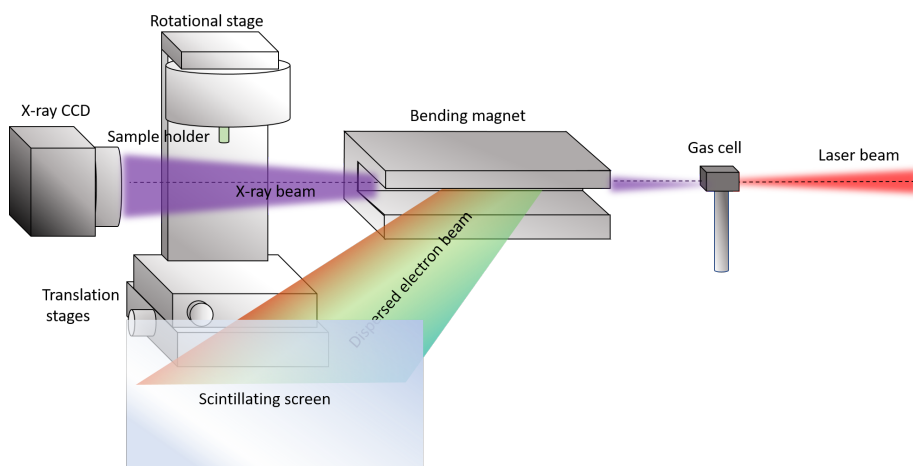


Figure 3.3: A simplified schematic representation of the experimental setup showing the most relevant components. The laser pulse enters the chamber from the right and is focused at the entrance of the gas cell. In the gas cell the electrons are accelerated and generate x-rays. The electrons and the x-rays co-propagate until the bending magnet, where the electrons are dispersed onto a scintillating screen. The x-rays continue to the sample, mounted in the sample holder. The sample holder is attached to two motorized translation stages, with a direction of motion perpendicular to each other. The x-rays are finally detected by the CCD that is positioned 1.8 or 2.8 m from the sample.

wires were mounted on translation stages between the gas cell and the bending magnet instead. The vacuum chamber operates at a pressure of roughly  $2.5 \cdot 10^{-4}$  mbar.

The electron energy was continuously monitored during all experiments and figure 3.2 shows the dispersed electron beam for 20 consecutive shots. The electron beam is dispersed by a bending magnet onto a scintillating screen, this means that higher energy electrons are bent less, corresponding to the left side of figure 3.2 while lower energy electrons correspond the right side. The exact electron energy values are not presented as this requires some calibration which was not done.

## Gas Target

The gas cell is made of aluminum with a drilled hole, creating a cylindrical cavity with a length of 6 mm. Before each experiment this hole is covered with some aluminum tape, a few hundreds of micrometer thick in total. Instead of having a pre-made hole in the foil for the laser pulse to pass through, a new hole is drilled using the laser at low energies in each experiment. This ensures that the laser is aligned to the hole and the size of the hole is the appropriate size to get the best gas density gradient. At the back of the gas cell a thin copper plate

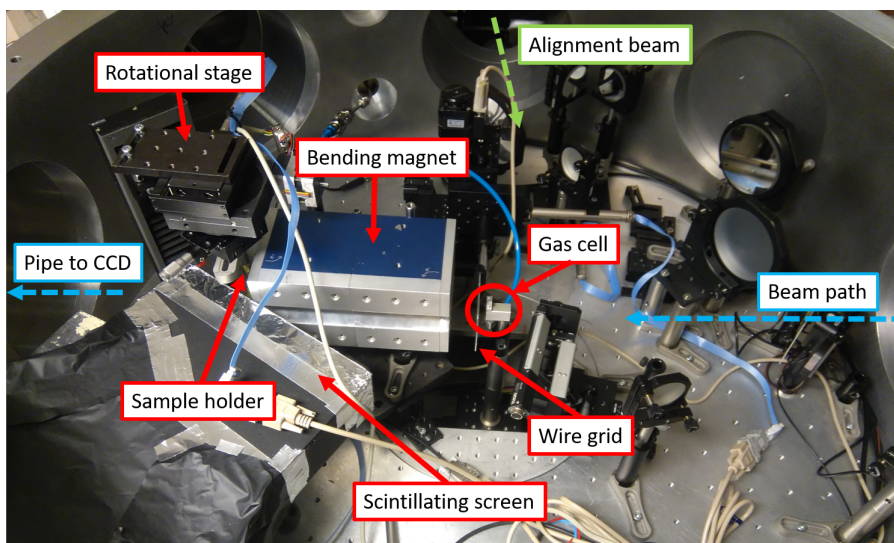


Figure 3.4: A photograph of the experimental setup.

is also added to the aluminum tape to prevent the drilled hole from growing too large. The focus of the laser is set at the cells entrance so the beam size is quite large at the gas cell exit and if it would drill a hole at that size it would degrade the gas pressure, the copper plate prevents this. The gas used is a mixture of helium and nitrogen, with a ratio of 1 % nitrogen at a pressure of roughly 0.3 bar, corresponding to an electron density of about  $1.4 \cdot 10^{19} \text{ cm}^{-3}$ , and is fed into the cell from below.

## X-Ray CCD

The x-ray detector used is an Andor iKon-L SO 936, a deep-depletion, back-illuminated CCD (BR-DD sensor) and 4-stage peltier cooling. Table 3.1 shows a specifications summary of the CCD and figure 3.5 shows the quantum efficiency curves. Both table 3.1 and 3.5 are taken from the specification sheet from Andor, available at their webpage.

The CCD is protected by a 250  $\mu\text{m}$  thick beryllium window and another such window is attached to the vacuum chamber where the x-rays exit. The CCD is not mounted on the chamber so there is a small section between the chamber and the CCD where the X-rays have to propagate in air (59 mm). The chip is cooled to  $-60^{\circ}\text{C}$  and is kept in vacuum. The transmission for a 500  $\mu\text{m}$  thick beryllium window and 59 mm of air is shown in figure 3.6 and these values are included in all simulations.

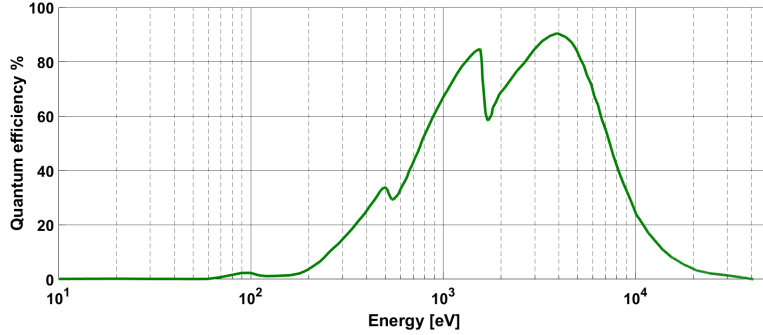


Figure 3.5: Quantum efficiency curve for the Andor iKon-L SO 936 in the energy range  $10 - 5 \cdot 10^4$  eV generated from data provided by Andor.

Active pixels	$2048 \times 2048$
Sensor size	$27.6 \times 27.6$ mm
Pixel size (W $\times$ H)	$13.5 \times 13.5$ $\mu\text{m}$
Active area pixel well depth	100,000 $e^-$
Maximum readout rate	5MHz
Read noise	2.9 $e^-$
Maximum cooling	-100 $^\circ\text{C}$
Frame rate	0.95 fps

Table 3.1: Specifications summary for Andor iKon-L SO 936, the x-ray CCD found in Andor’s user manual.

### 3.3 Source Size Determination

To determine the source size, a grid of tungsten wires were placed in a manufactured mount in the form of a aluminum plate with a rectangular slit. This was to make sure there were more wires available during the experimental run if one would be miss-aligned, destroyed, damaged or badly manufactured.

The mount was then mounted on two translation stages to allow for alignment in the horizontal and vertical plane. It was positioned 1.6 cm from the source and 1.8 m from the detector, resulting in a magnification of  $M = 181$ . The idea was to place the wire as close to the source as possible without breaking it as this would increase the effect of the source size. This was also the reason as to why the choice of material was tungsten as it has a very high melting point.

Two different types of wires were used, both tungsten, but one with a diameter of 25  $\mu\text{m}$  and one of 50  $\mu\text{m}$ .

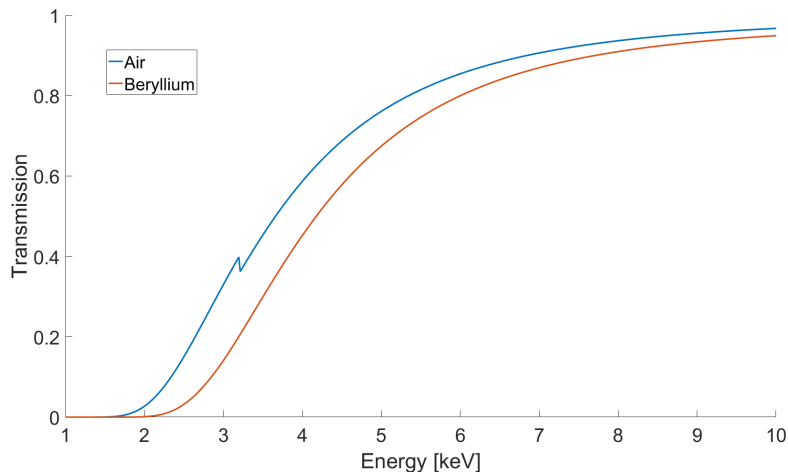


Figure 3.6: The transmission of 500  $\mu\text{m}$  Beryllium (orange) and 59 mm of air (blue) calculated at "x-ray interactions with matter" [24].

### 3.3.1 Simulation

In order to determine the source size, a simulation is needed of the expected diffraction pattern for different source sizes. The experimental data is then fitted to this simulation, determining the size of the source.

The equation used to calculate the intensity in the detector plane when illuminating a wire is equation 2.32 [14]. A 3-dimensional grid is created to hold the coordinate systems of the detector  $x_d$ , the object  $x$  and the source  $x_s$ .

The X-ray spectrum is calculated from equation 2.13 for a critical energy of 3 keV and sampled to obtain the relevant wavelengths, the calculation of 2.32 is then looped over two variables. The outer loop are for different source sizes and the inner loop are for different wavelengths.

The quantum efficiency is given by tabulated values from figure 3.5 and the calculated intensity is multiplied by these values for each corresponding wavelength. The same procedure follows for the transmission of x-rays through beryllium and air, with values calculated from "x-ray interactions with matter" [24]. This is done for each wavelength and the result is, after integrating two variables, a vector for each wavelength that is concatenated to form a matrix. This matrix then has the intensity as a function of  $x_d$  in one dimension and wavelengths in the other. This dimension is multiplied by the weights from the normalized wavelength spectrum and then integrated with respect to the wavelengths. The final result is thus a weighted average of the intensity over the detectors coordinate system  $x_d$ .

As the integration has to be done over three variable,  $x$ ,  $x_s$  and the wavelength,  $\lambda$ , it was done numerically using MATLAB's built-in *trapz* function that approximates the integral using the trapezoidal method. This method divides



the area into trapezoids, computes these area and sums the result. For  $N + 1$  equidistant grid points the approximation is [25]

$$\int_a^b f(x)dx \approx \frac{b-a}{2N} \sum_{n=1}^N (f(x_n) + f(x_{n+1})). \quad (3.1)$$

This is the most accurate second-ordered method and it usually performs very well, with fast convergence when the solution is periodic as the error tends to cancel out [26].

Figure 3.7 and 3.8 show a test simulation for a wire thicknesses of 10  $\mu\text{m}$  and 50  $\mu\text{m}$ . The source-object distances are 1 cm and 1 mm respectively, object-detector distances are 3 m and 0.5m respectively, and it is simulated for source sizes ranging from 1 to 2.2  $\mu\text{m}$  in steps of 0.4  $\mu\text{m}$ . The transmission function is also shown, mainly to illustrate that a wire will transmit more at its edges and the transmission function becoming more parabolic in nature, especially if the wire is thinner. For a 50  $\mu\text{m}$  thick tungsten wire with x-rays ranging from 1 keV to 10 keV the transmission is not significant, but there is a small effect, as can be seen from the transmission function in the left graph of figure 3.8. The computational domain only includes half the wire to save time and space as the other half will be symmetric. Another reason for this is that the trapezoidal method does not converge is there's too few grid points (or rather, the spacing between them is too large) and by taking advantage of this symmetry the computation becomes more stable. Having the wire very close to the source increases the effect of the source size, separating the different lines more, making for an easier fit with experimental data. This is not feasible, as the source is inside the gas cell where there is no room for a wire. The effect is demonstrated when comparing figure 3.7 and 3.8. As a conclusion, placing the wire as close as possible to the source without destroying it would yield the best source size resolution, which based on these simulations, is expected to be on the order of 1  $\mu\text{m}$ .

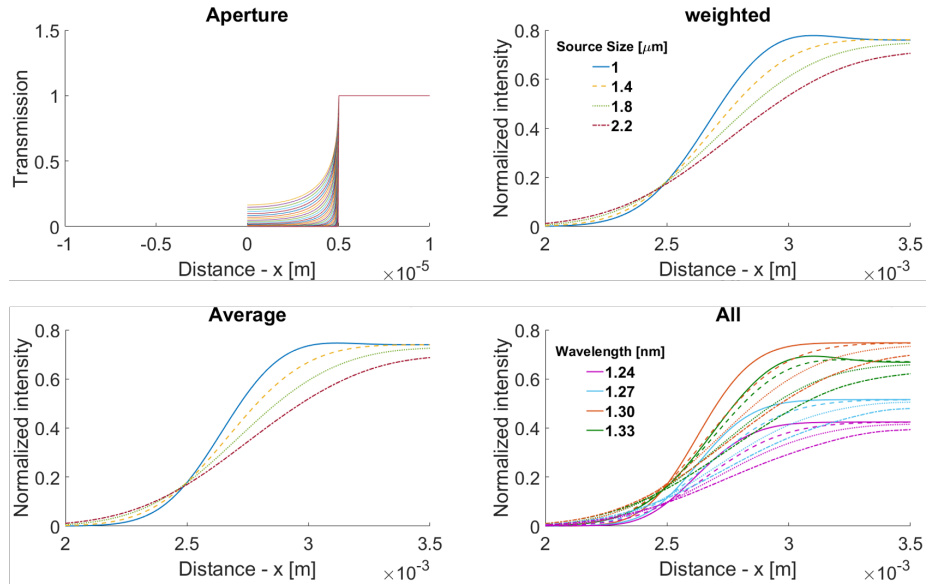


Figure 3.7: Simulation for a 10  $\mu\text{m}$  thick tungsten wire with a source-object distance of  $r_1 = 0.001$  m and object-detector distance  $r_2 = 0.5$  m. Top left shows the transmission function of the wire for different wavelengths. Note that this only shows half the wire, due to the symmetry only this side is calculated. Top right shows the result from the weighted integration with respect to the spectrum for different source sizes. Bottom left shows the unweighted average and the bottom right shows a few of the wavelengths (numbers in nm) for the different source sizes (indicated by differently dashed lines) before weighting or averaging.

### 3.4 Propagation and Phase-contrast Simulation

A script was written to simulate the propagation of x-rays, with the purpose to find the best experimental parameters to resolve objects of different sizes.

An object is defined by its transmission function  $q(x, y)$  [27]. In this simulation there are two objects, a cylinder and a sphere defined by the thicknesses

$$\begin{aligned} t_{sphere} &= 2\Re(\sqrt{r_1^2 - (x - x_1)^2 - (y - y_1)^2}) \\ t_{cyl} &= 2\Re(\sqrt{r_2^2 - (x - x_2)^2}) \end{aligned} \quad (3.2)$$

with radius  $r_1, r_2$  and a position of  $(x_1, y_1), (x_2, y_2)$  relative the origin.

Using the thickness in the expression of the transmission function, we have

$$q(x, y) = e^{-k(t_{sphere}(x, y) + t_{cyl}(x, y))(\beta + i\delta)}. \quad (3.3)$$

Calculating the Fresnel diffraction using equation 2.18, that equation can be rewritten in the form of a convolution and Fourier transforming this results in

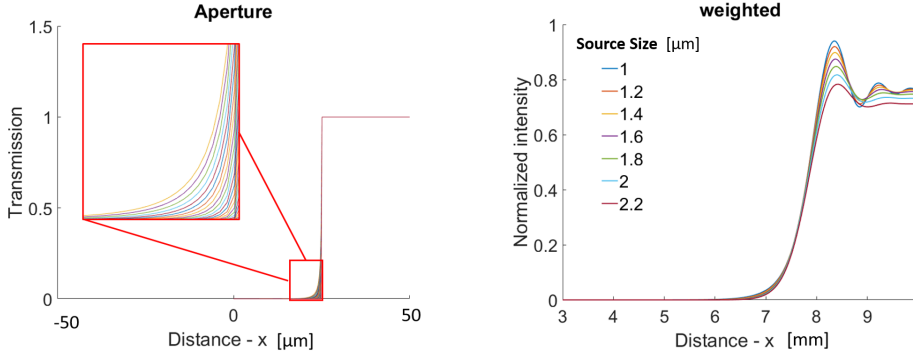


Figure 3.8: Simulation for a 50  $\mu\text{m}$  thick tungsten wire with a source-object distance of  $r_1 = 0.01$  m and object-detector distance  $r_2 = 3$  m. Left figure shows the transmission function, for a 50  $\mu\text{m}$  thick wire it is significantly less, compared to a 10  $\mu\text{m}$  wire but zooming in shows that it should still be taken into consideration. This simulation is close to the actual setup except that the detector is positioned at  $r_2 = 1.8$ . The lines for different source sizes are very close and it might be hard to fit experimental data to sub-micrometer accuracy but an accuracy of about 1  $\mu$  is reasonable to expect.

a multiplication [27]. This is to make use of the Fast Fourier Transform (FFT) and the equation used is then

$$U = \mathcal{F}^{-1} \left( \mathcal{F} \left( U_0 q(x, y) \right) \mathcal{F} \left( \frac{1}{iz\lambda} e^{\frac{ik}{2z}(x^2+y^2)} \right) \right) \quad (3.4)$$

where  $U_0$  is the constant, unperturbed wave field.

After this, some *speckle noise* is added to the image and it is blurred with a Gaussian filter. The noise is calculated as  $I = I_0(1 + n)$  where  $I_0$  is the clean image and  $n$  is a uniformly distributed random variable, see MATLAB's reference page for more information. The blurring is to simulate the blurring due to the extended source size and to an extent, the point spread function of the CCD [27]. The point spread function generally describes the response on an optical system to a point object or point source. In this case there are no optics but a photon incident on the detector might give an output signal that spreads out over several pixels, which is referred to as the point spread function here [27]. This has not been measured however and a blurring radius was chosen to simulate only the source size and a small additional blurring. The size was decided so that the radius of the Gaussian filter is on the order of  $d \frac{r_2}{r_1}$ , as mentioned in section 3.4 to simulate the blurring from the source size, then increasing it slightly to  $1.1d \frac{r_2}{r_1}$ .

The image is also scaled a factor  $M$  to take into account the magnification and as the detector also has a finite area, the image is cropped if it is too large to fit on the detector.

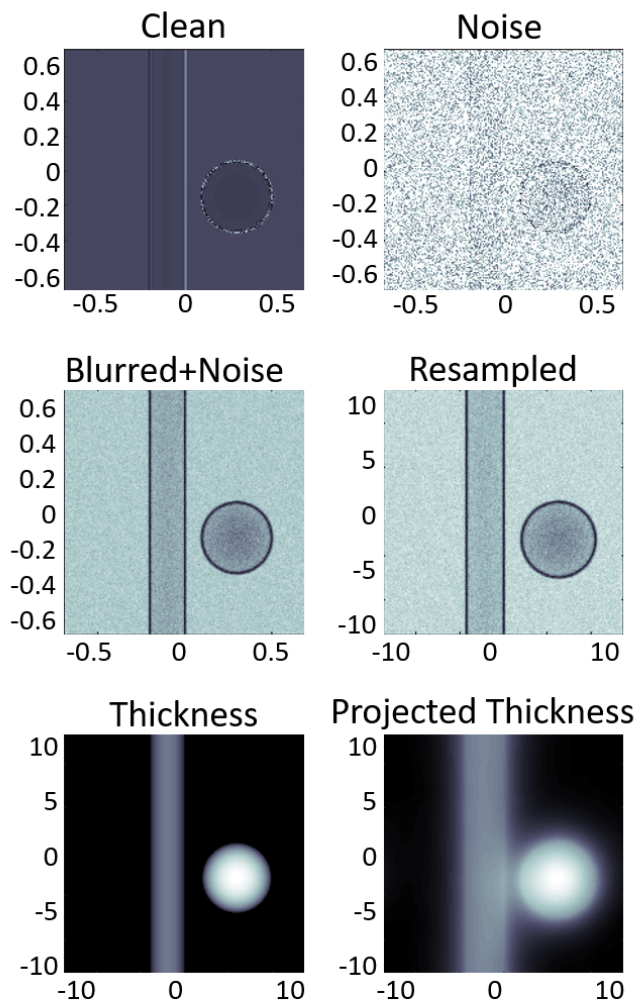


Figure 3.9: Figure showing the results of simulating Fresnel diffraction and calculating the projected thickness. It shows the **clean** image, i.e. just the intensity at  $z = r_2$ , the fringes are very closely spaced and barely distinguishable, adding **noise** and **blurring** makes it clearer and the edge enhancement effect is noticeable. The **re-sampled image** is scaled by a factor  $M = 20$  due to the magnification and re-sampled to the pixel size of the detector, simulating a detected phase-contrast image. The bottom left image shows the defined **thickness** of the simulated object and the bottom right shows the calculated **projected thickness** using the single material phase-retrieval algorithm on the re-sampled image. Values are in mm.

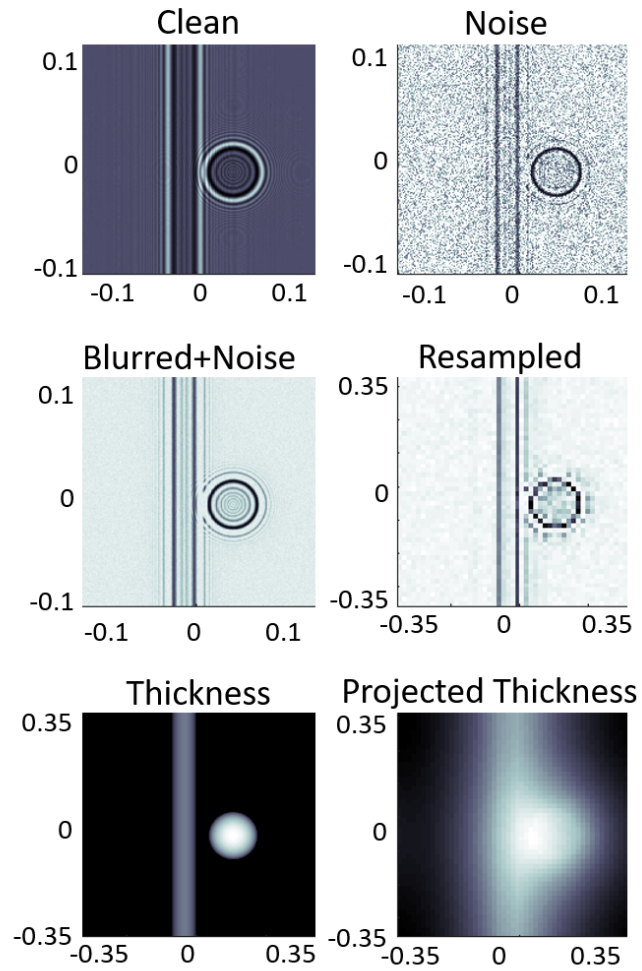


Figure 3.10: Decreasing the magnification to  $M = 3.5$  results in the objects taking up a lesser area of the detector, making the re-sampling more prominent, therefore also degrading the results of the projected thickness. Values are in mm.

The detectors pixel size is also finite and thus the whole image needs to be re-sampled to the pixel size of the detector, taking the simulation pixels that fit in one pixel of the detector and averaging these.

The polychromaticity of the source is also simulated, integrating the image over the X-ray spectrum with wavelength dependant index of refraction.

The setup also has two beryllium windows the x-rays need to pass through, the transmissions of these (figure 3.6) are also taken into account and the x-rays also propagate a small distance in air which is taken into account in the same way. These transmissions were calculated at "x-ray interactions with matter" [24] and interpolated to fit the desired spectrum.

The algorithm described in section 2.6.2-2.6.3, Paganins algorithm for single material phase-retrieval, can be used to calculate the projected thickness of the experimental x-ray images as well as the simulated ones.

Figure 3.9 shows the acquired images from the simulation for a sphere and a cylinder of mylar of radius 100 and 200  $\mu\text{m}$ , respectively. The objects are at a distance of  $r_1 = 0.1$  m from the source, that has a size of 3.5  $\mu\text{m}$ . The detector is 2 m from the object and the magnification is thus  $M = 21$ . The simulation grid points have a size of 0.4  $\mu\text{m}$  and the simulation grid has  $9 \cdot 10^6$  grid points in a square. These grid points are then averaged into larger grid points corresponding to the cameras pixel size, which is referred to as "re-sampling" here.

The image titled "clean" shows the Fresnel diffraction at  $z = r_2$ , the images titled "noise" and "blurred+noise" shows the effect of adding noise and blurring the image. Since the simulation pixels are smaller than the detectors pixels the re-sampled image have lower resolution. At this distance the re-sampling does not make a big difference as the objects cover a big area on the detector and remains well resolved. The image titled "thickness" shows the objects thickness, i.e equation 3.2. The bottom right image, titled "projected thickness" shows the results of calculating the projected thickness using the single material algorithm 2.43 on the re-sampled image. The projected thickness is changed as the image is subjected to noise and blurring, along with the loss of resolution of re-sampling. Running the same simulation again but without noise, blurring and re-sampling results in figure 3.11 which shows a much better result for the projected thickness as it looks very similar to the true thickness.

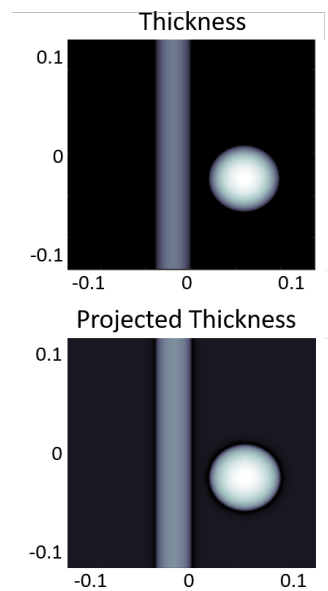


Figure 3.11: Removing the noise and blurring improves the result from the single material phase-retrieval algorithm as the projected thickness (bottom) is closer to that of the true thickness (top). Values are in meters.

Decreasing the magnification to  $M = 3.5$  and adjusting the position of the objects to fit the screen while keeping their sizes results in figure 3.10. It is obvious that the re-sampling has a bigger impact here as the objects are less magnified and cover a much smaller amount of pixels and the results in a poor projected thickness image.

The purpose of these simulations were to find a good distance between the source, sample and detector. It is obvious that one wants to make use of as many pixels as possible, but other things have to be taken into consideration as well. The wave needs to propagate far enough for the phase to develop into detectable intensity modulation, but the camera can't be too far away as this significantly reduces the flux. Having the sample close to the source results in better magnification but it also blur the image more due to the source size. Further, the point spread function also has an impact on the optimal distance. In the end, the distances with the best magnification and easiest setup was used as this seemed to have the biggest impact in the simulations.

## 3.5 Phase Contrast

The rotational stage was calibrated to move in 1 degree increments and mounted behind the bending magnet, 30 cm from the source. The CCD was positioned at two different distances, either 2.8 or 1.8 m from the source.

The samples were mounted on a dosing needle attached to the rotational stage. This was then aligned to have an axis of rotation as central as possible with respect to the beam using an alignment laser and by looking at the shadow on the CCD.

Having the CCD further away increases the magnification and the objects cover a larger area of the detector, improving the resolution. There is a trade-off however, as the flux decreases due to the divergence of the X-ray beam. To improve the contrast of the images, they had to be averaged, so several images were taken at each angle, and when the CCD is further away more images had to be averaged.

The samples used were a fishing line, 100  $\mu\text{m}$  in diameter, an unspecified fly that was found in the authors kitchen lamp (shown in figure 3.12), a bee head kindly donated by Elisa Rigosi from the Biology Department at Lund University and another smaller fly.

### 3.5.1 Numerical Implementation

The implementation of the phase-retrieval algorithm, i.e equation 2.43, was done in MATLAB.

First, the raw images need to be treated. The image,  $I$ , is calculated as

$$I = \frac{I_0 - I_d}{I_f - I_d} \quad (3.5)$$

where  $I_d$  is a dark image, i.e an image with nothing but the background noise.  $I_f$  is the so-called flat image, an image with X-rays but no object and  $I_0$  is the raw x-ray image, i.e the phase-contrast image. As the X-ray beam have an inhomogeneous intensity distribution there will be a gradient over the image and this will be accounted for when dividing by the flat field.

Equation 2.43 assumes a monochromatic source and one has to average over the wavelengths in the X-ray spectrum, if it is a polychromatic source [1]. The spectrum was assumed to have a critical energy of 3 keV, calculated using equation 2.13. Using calculated values for the refractive index [24] and interpolating these into wavelengths that fit the chosen spectrum one can find the average refractive index of the sample. In the case of insects the material was assumed to be chitin,  $C_8H_{13}NO_5$ , a polymer very common in nature that is a main component in exoskeletons. The exact composition of the fishing line was not known but is assumed to be mainly mylar,  $C_{10}H_8O_4$ , a widely used polyester.

The quantum efficiency of the detector is also taken into account in the same manner, interpolating to find values that fit the desired spectrum and multiplying the intensity to get the detected intensity.

As there are quite a few images this is done in a looping script that reads images with numbered file names, processes them and calculates the projected thickness and writes them as gray scale images with the correct numbering.

### 3.6 Alignment

The process of averaging the images is not a simple matter of just adding them together. As there is some laser pointing fluctuations, i.e the focus of the laser jumps around a bit inside the gas cell from shot-to-shot, the X-ray source will also move from shot to shot. As the source moves, the image on the detector will move, thus, resulting in unaligned images.

The solution to this was to introduce a reference object that is stationary and in the same plane as the object. Here, a tungsten wire was used as it creates a sharp shadow and is easier to align and whenever the sample moves due to the laser pointing fluctuation the reference point will move by the same amount. Thus by aligning by the reference point it will also be aligned with respect to the object.

A script was written to align these images. Doing this automatically was problematic due to the noise and to improve this, the images are first filtered

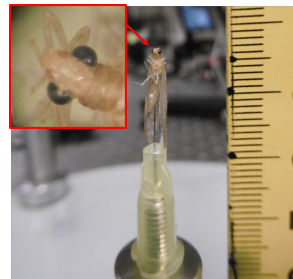


Figure 3.12: Photograph of one of the samples used, a fly found in a kitchen lamp. As the magnification for the setup was slightly too large only the neck, head and part of the upper body were imaged.



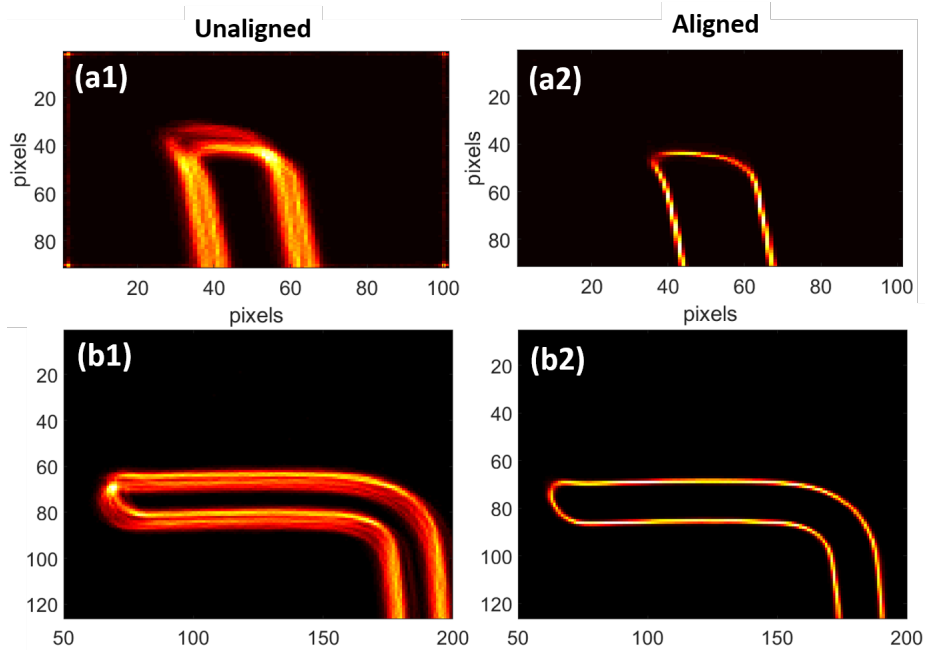


Figure 3.13: The sum of all cropped images before (a1, b1) and after alignment (a2,b2) after using an edge-detection algorithm. The reference objects was a straight 50  $\mu\text{m}$  tungsten wire (a) and an "L-shaped" tungsten wire (b) of the same thickness. The latter geometry was used as the alignment script performs better with a reference object that has the same "amount" of edge in both the vertical and horizontal plane.

using a Gaussian filter. The image are then cropped to show only the reference object. Then an edge detection algorithm was used, this was a built in function in MATLAB that uses the Sobels method that finds edges using the Sobel approximation to the derivative, see MATLABs reference page for more details on the *edge* function.

Choosing one image to be fixed, all other images are aligned to this one. This was usually just a shot with high flux so the shadow was as sharp as possible. After the image is cropped, filtered and only the edge is visible, the normalized cross-correlation between the reference image and the current image is calculated. Finding the maximum in this matrix and subtracting the size of the image gives the translation difference in pixels. The uncropped image is then translated by the same amount of pixels and averaged. Figure 3.13 shows a typical result of this process, showing the sum of all images that are aligned, and the sum of the unaligned images.

As it takes a few hours to take all the shots, the pointing of the laser has time to drift quite a bit. This can be seen in figure 3.13 as well but this effect

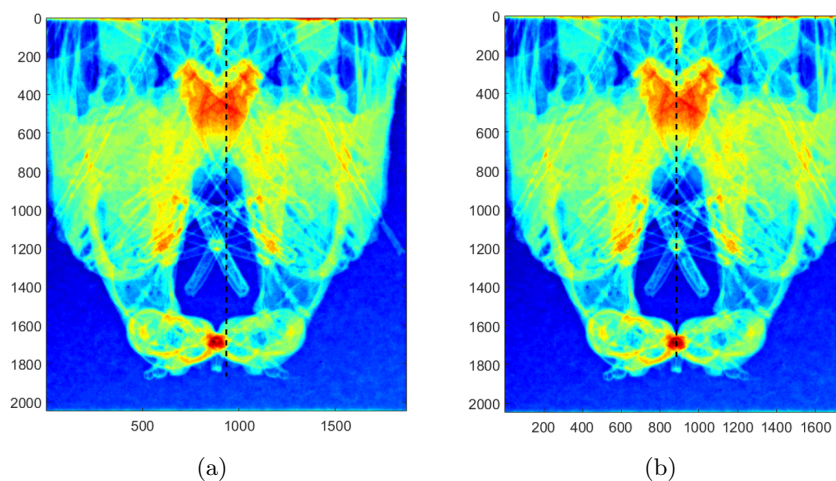


Figure 3.14: Comparison between the unsymmetrical image (a) and the symmetrical (b) after centering it. Image (a) was created by summing an image taken at 0 degrees and 180 degrees of a fly. A dashed line in the centre is used to manually align the centre of the image by cropping it, resulting in image (b). The choice of colorscale is just to aid in this process and is of no other importance in this context.

is corrected by the same procedure so it did not pose an additional problem.

A problem was discovered when using a reference object that has more edge along one direction than another. The script tended to weight the fitting and preferred to fit in one direction instead of both. One solution was to crop the image more to reduce the amount of edge in one direction but this leaves fewer pixels to fit against. The result was that the script was not flawless and some images had to be realigned afterwards. This could probably be solved by weighting the cross-correlation matrix but instead a different reference object was used, a tungsten wire bent in an "L" shape that worked better, this is shown in figure 3.13. With this reference object no manual alignment was required and all images were directly aligned by the automated script.

### 3.7 Tomography

The tomography was done using the images showing the projected thickness, calculated using 2.43, taken at different angles. The method used was a parallel beam geometry, i.e. the process described in section 2.6.3 with a ramp-filter. The process is also called filtered backprojection as mentioned before, as it includes a linear high-pass filter.

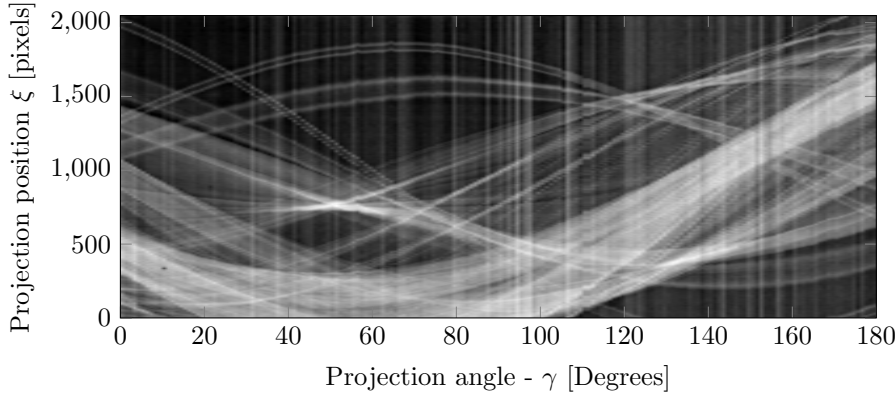


Figure 3.15: A sinogram of a fly, 36 pixels down from the top over 180 angles with 1 degree increment. The intensity from shot to shot varies and this is very visible here as there are multiple vertical streaks. The choice of name also makes itself obvious as there is a clear sinusoidal pattern in the image.

### 3.7.1 Numerical Implementation

The tomography was done by an automated script that reads the calculated projected thickness images in numerical order, sorted by the angle of the object. Using a 1 degree increment, this results in 180 images but the last image is not necessary as it is the same image as the first one but flipped vertically. These images were instead used to determine the center of rotation however. Adding the first and last image together to find the centre of symmetry in the combined image also gives the centre of rotation. All images are then cropped to have this dimension and a centralized rotation with respect to the image. Figure 3.14 shows the result of this process for a fly sample.

The next step is to create the sinograms, i.e  $p_\gamma(\xi)$  and this can be done by simply stacking all the images, that would be a matrix with the dimensions  $N_x \times N_y \times N_{angles}$ , where  $N_x, N_y$  are the image size and  $N_{angles}$  the number of angles. Reshaping this matrix to a  $N_x \times N_{angles} \times N_y$ , this can be thought of as a stack of  $N_y$  images with dimensions  $N_x \times N_{angles}$  and these are the sinograms. Figure 3.15 shows a typical sinogram obtained by this method. The vertical lines across the image originate from the shot-to-shot intensity variations. During this experiment 5 shots were taken at each angle (corresponding to the x-axis in the image) and despite averaging they are still very visible.

Once all the sinograms have been calculated and are readily available the reconstruction can begin. This is done using MATLAB's built in function "iradon" that calculates the inverse radon transform with a Ram-Lak filter. This is the same as equation 2.65 and acts as a high pass ramp-filter. It takes as input a matrix where the columns are the parallel beam projection data and the rows correspond to the angles of which the projection was taken, i.e the sinograms. One also needs to specify the angle increment and this is taken as a second

---

input. This calculates  $f(x, y)$  or  $\mu(x, y)$ , i.e the distribution of the linear attenuation in a cross-section of the sample and as such this needs to be done for all sinograms to get the full reconstruction. This results in  $N_y$  images which are saved into a TIF stack for convenience.

## Chapter 4

# Results

This section shows the results gathered during experiments and calculations. It contains the calculated projected thickness images, phase-contrast images, the result of the source size measurement, calculated tomography images and 3D rendering of the samples.

### 4.1 Source Size Determination

Figures 4.1 and 4.2 shows the results of the code to determine the source size, discussed in section 3.1.1 together with the experimental data. Two tungsten wires were used, one with a diameter of 25  $\mu\text{m}$  and one with 50  $\mu\text{m}$ . The data was averaged in the direction of the wire to increase the signal to noise ratio after subtracting the flat field. The data was also smoothed using locally weighted scatterplot smoothing (LOWESS) to allow for easier fitting, see MATLABs reference page for more information on this method. A first fit is made by minimizing the RMS value and positioning the experimental data at that curve's midpoint. After the initial guess, manual fitting is allowed by a small slider in the graphics window that allow translation of the experimental data. These results suggest a vertical source size of 2.5  $\mu\text{m}$  and a horizontal source size of 3.5 - 3.7  $\mu\text{m}$ . This method is accurate to within 20 % [14], resulting in a final vertical size of approximately  $3.6 \pm 0.72 \mu\text{m}$  and a horizontal size of  $2.5 \pm 0.5 \mu\text{m}$ .

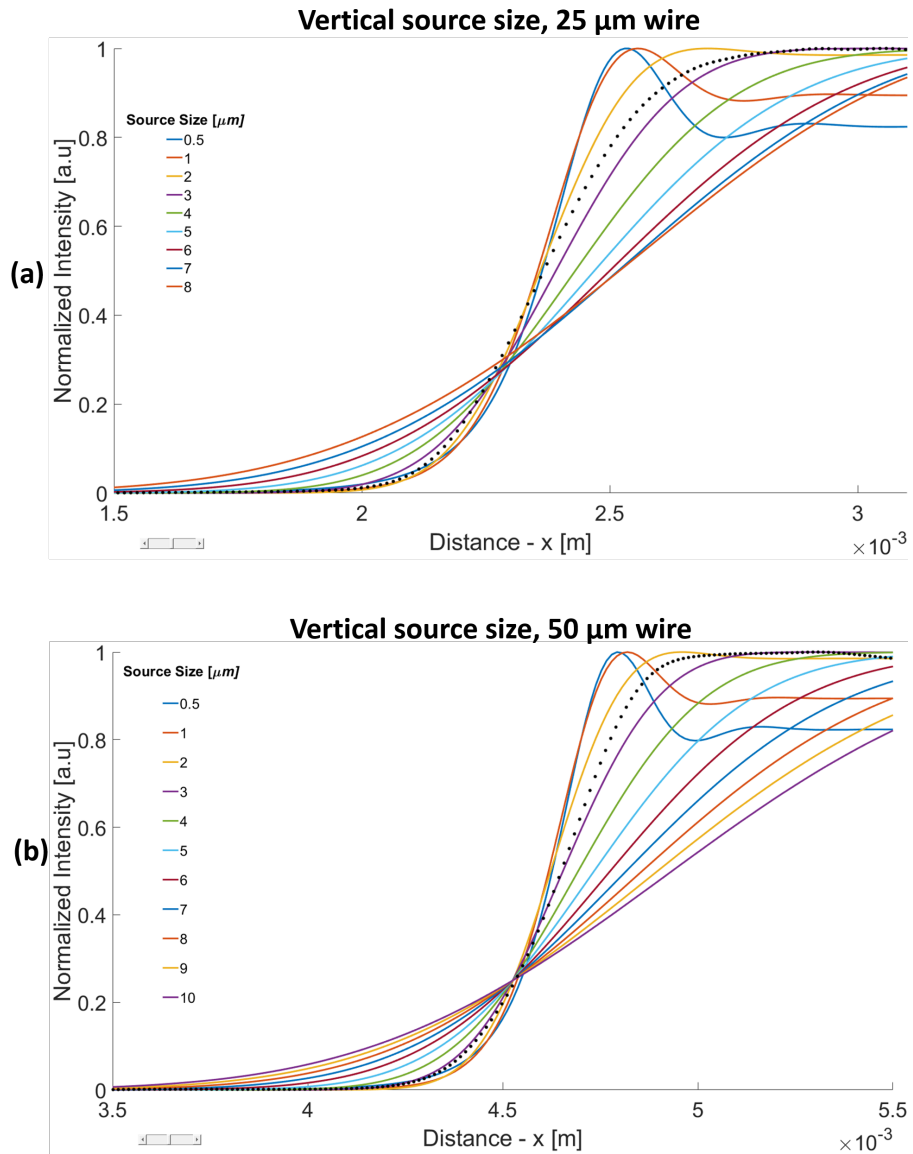


Figure 4.1: Result of fitting the experimental data (dotted line) to the simulated data for source sizes ranging from 0.5 to 10  $\mu\text{m}$ . The experimental data was taken using a 25  $\mu\text{m}$  (a) and a 50  $\mu\text{m}$  (b) thick tungsten wire mounted in the horizontal direction, giving a measurement of the vertical source size with a best fit for a source size of about 2.5  $\mu\text{m}$ . In (a) source sizes above 8  $\mu\text{m}$  were not simulated

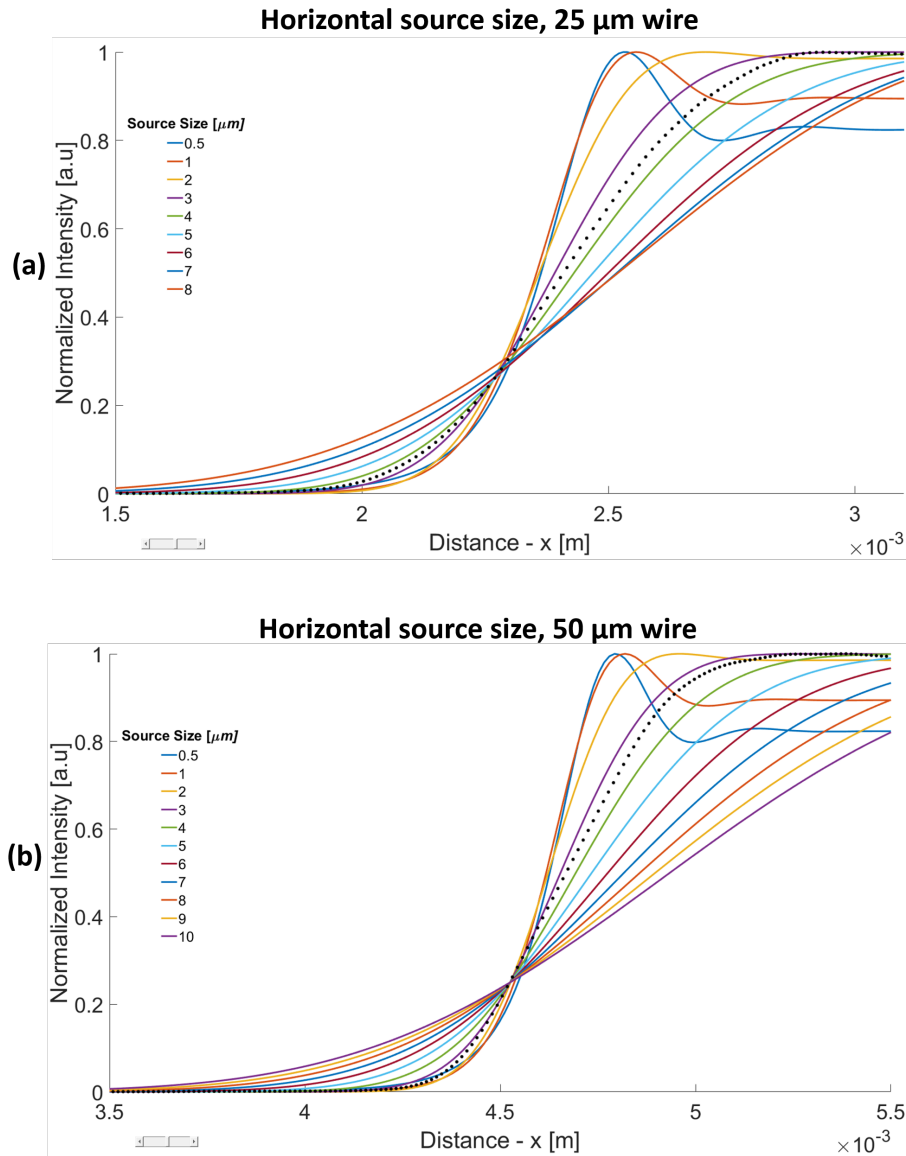


Figure 4.2: Result of fitting the experimental data (dotted line) to the simulated data for source sizes ranging from 0.5 to 10  $\mu\text{m}$ . The experimental data was taken using a 25  $\mu\text{m}$  (a) and a 50  $\mu\text{m}$  (b) thick tungsten wire mounted in the vertical direction, giving a measurement of the horizontal source size with a best fit for a source size of about 3.4  $\mu\text{m}$ . In (a) source sizes above 8  $\mu\text{m}$  were not simulated

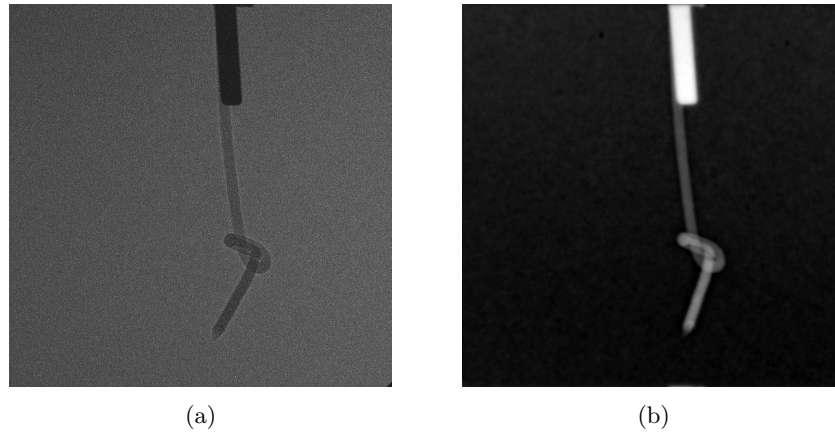


Figure 4.3: The raw phase-contrast image of a knotted, 100  $\mu\text{m}$  fishing line (a), mounted to a dosing needle. Calculating the projected thickness using equation 2.43 resulted in (b). The fishing line was assumed to be made of mylar.

## 4.2 Phase Contrast

Figure 4.3 shows the raw phase-contrast image of a knotted fishing line with a thickness of 100  $\mu\text{m}$  along with the calculated projected thickness image using equation 2.43. These images were not aligned before being averaged as there was no reference object present and, to increase the signal-to-noise ratio, 5 shots were taken at each rotation. The result is still relatively good, but the effect will not be noticeable as there's a lack of finer detail in this sample. Figure 4.4 shows the raw phase-contrast and projected thickness image of a 100  $\mu\text{m}$  thick fishing line with a double knot. These images were averaged over 10 shots to offset the reduction in flux as the CCD was moved back to increase the magnification. The laser pointing fluctuation and the laser drift were not corrected in these images either. Looking at figure 4.4 a) there is a clear effect of edge enhancement that comes from the abrupt change in refractive index as discussed in section 2.3.

Figure 4.5 shows the result of the calculated projected thickness algorithm for the fly specimen compared to the raw phase-contrast image used to calculate the projected thickness. This image has been aligned and averaged over 5 images. The material was assumed to be chitin,  $C_8H_{13}NO_5$  and values for the refractive index for the spectrum shown in figure 2.5 with a critical energy of 3 keV was obtained from "x-ray interactions with matter" [24]. Some of the finer details are lost when calculating the projected thickness, such as small hairs.

Validation of the algorithm used to calculate the projected thickness was done by summing the image in figure 4.3 along the direction of the 100  $\mu\text{m}$  fishing line and calculating the projected thickness. This is compared to the analytic normalized projected, figure 4.6 and the overall resemblance is good.

Figure 4.7 shows the projected thickness image of a bee head together with



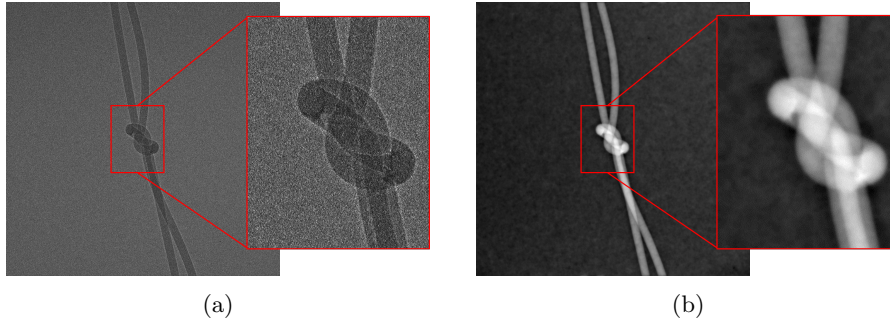


Figure 4.4: The raw phase-contrast image of a 100  $\mu\text{m}$  thick fishing line with a reef knot (a), mounted to a dosing needle. Calculating the projected thickness using equation 2.43 resulted in (b). The fishing line was assumed to be made of mylar. The projected thickness image shows a gradient across the wire, hinting at a cylindrical shape, information that is not clearly visible in the raw phase-contrast image. Figure a) also shows some edge enhancement as there is a bright fringe around the edge.

the raw aligned and averaged phase-contrast image. The sample was rather fresh and as the chamber was pumped, the low pressure caused damage to the head, making it useless for tomography as some parts were moving during the rotation. It was attached using a drop of wax that can be seen at the top of the images.

Another sample was also used, a smaller fly that is shown in figure 4.8 along with its projected thickness image aligned and averaged over 5 shots. Unfortunately, this specimen was destroyed as there was a triggering error and the gas injection failed. This allowed the laser to propagate unperturbed all the way to the fly, hitting it with close to full intensity and destroying it. Despite this, enough shots were taken to calculate the projected thickness for one angle.

### 4.3 Tomography

The tomography was done using a parallel beam geometry, using the inverse Radon transform built in MATLAB with linear interpolation and a Ram-Lak filter.

Figure 4.9 shows the tomographic reconstruction of the knotted fishing line. The slice reconstructed is located in the middle of the knot. These images were taken at 5 degree increments and the result of this can be clearly seen as it has notable artifacts streaking across the image. Using smaller increments would reduce this effect.

Figure 4.10 shows the result from the tomographic reconstruction of a bee head. During this run there was some problem with the flux which became rather low at times. The sample also moved during the process and one of the

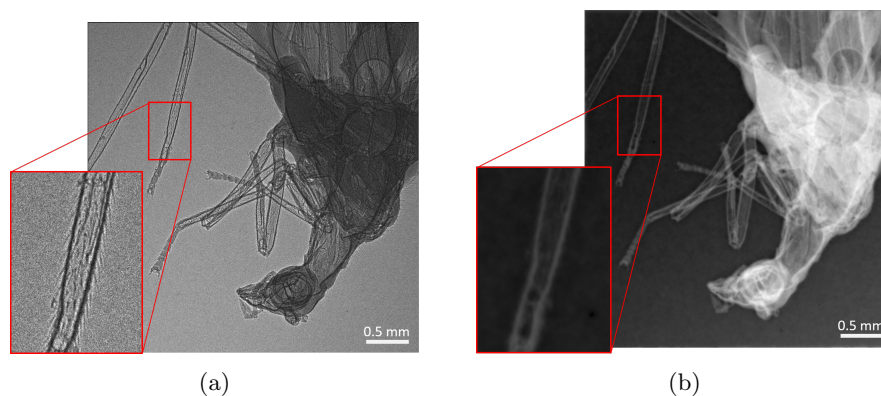


Figure 4.5: Comparison between a projected thickness image of a fly (b) with the raw, aligned and averaged phase-contrast image (a). The contrast between the background and the middle part of the leg is much better compared to the raw phase-contrast image. However, finer details are lost, such as small hairs on the leg.

tendrils moved out of the frame. These things combined resulted in a rather poor reconstruction.

Figure 4.11 shows the results of a tomographic reconstruction of a fly at different cross-sections with increasing height ranging from (a) to (d). The raw phase-contrast images used to calculate the projected thickness for this sample were taken over 180 degrees with 1 degree increment and averaged over 5 shots at each angle. A circular pattern can also be seen in the background due to the nature of the transform as only linear interpolation was used. This creates artifacts from the interpolation error due to the regridding issue mentioned in section 2.6.2.

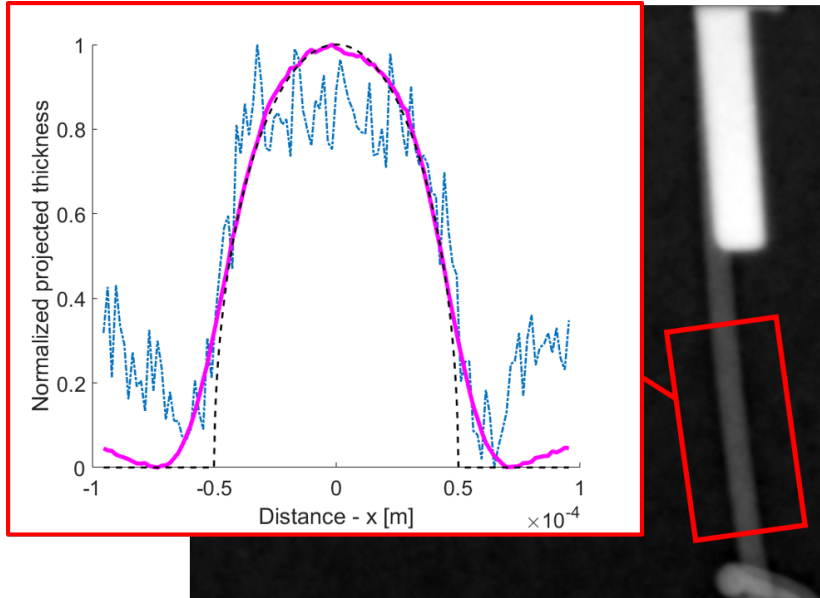


Figure 4.6: A comparison of the analytic normalized projected thickness of a 100  $\mu\text{m}$  mylar wire (black dashed line), the raw phase-contrast data (blue dot-dashed line) and the calculated projected thickness (purple solid line) from figure 4.3. The calculated projected thickness is close to the analytic but fails slightly at the edge.

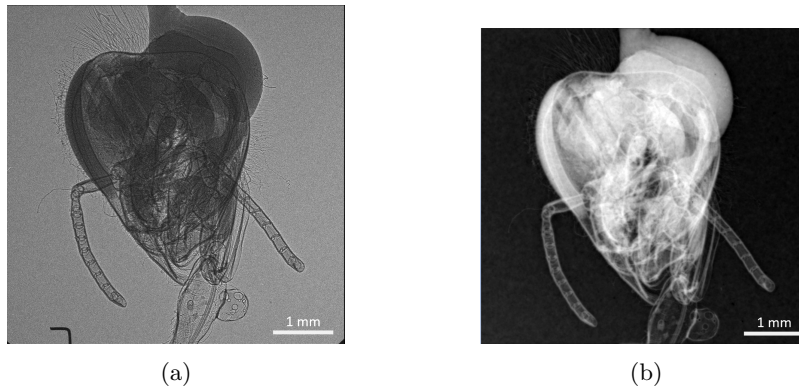


Figure 4.7: Projected thickness image of a bee head b) along with the aligned and averaged raw x-ray phase-contrast image a). The reference object has been cropped out in b) for better colormap scaling.

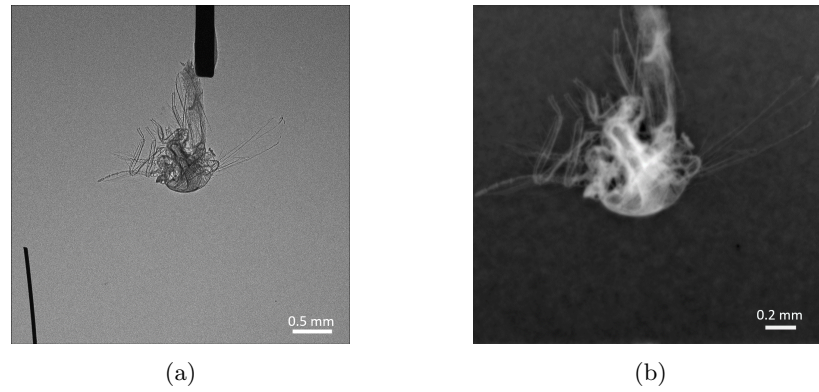


Figure 4.8: Projected thickness image of a smaller fly (right) along with aligned and averaged raw phase-contrast images (left).

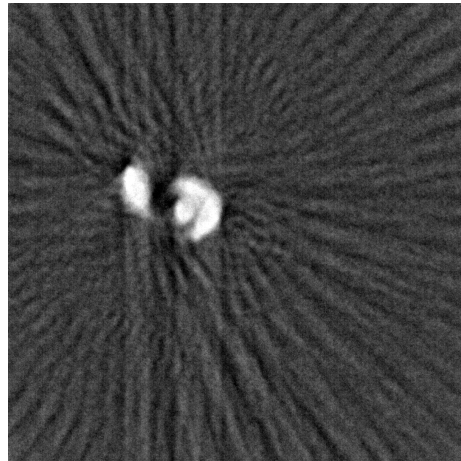


Figure 4.9: Tomographic image of the fishing line with a single knot, created from the projected thickness images, such as figure 4.3. These projections were taken with a 5 degree increment, resulting in a worse reconstruction compared to the reconstruction of the fly, which had projections taken at 1 degree increments.



Figure 4.10: Tomographic image of a bee's head (right) reconstructed at the location indicated by the dashed line from the projected thickness images (left).

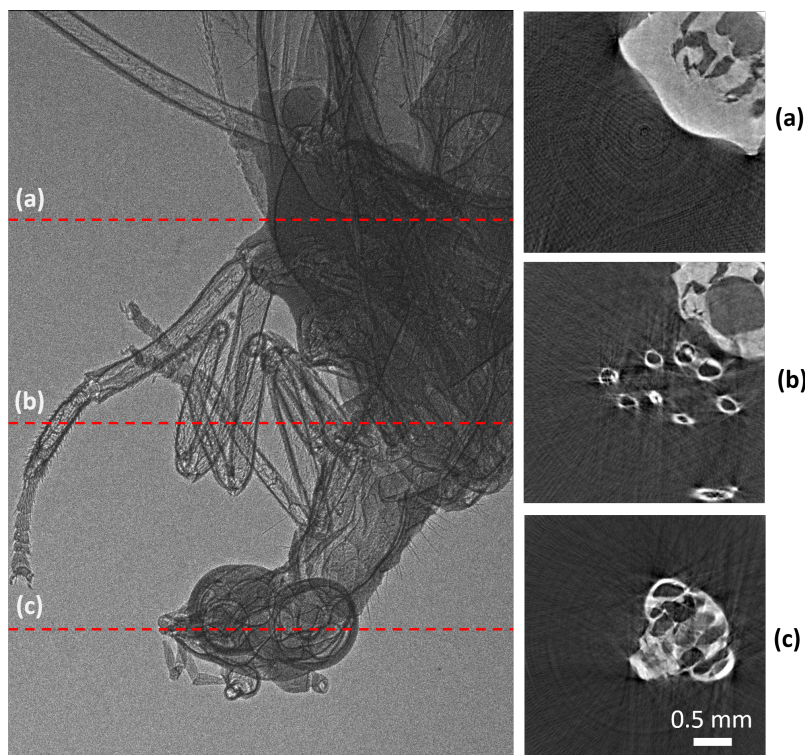


Figure 4.11: Tomographic images of the fly shown in figure 3.12. Figure (a) shows part of the body, the wings are too far out to be reconstructed. Figure (b) shows the neck along with some legs and (c) shows the head. Note that the length scale only applies to figures (a), (b) and (c). The raw phase-contrast image (left) has a different scale.

## 4.4 3D Rendering

The open source software 3D slicer was used to create a 3D volume rendering from the tomographic images, the software can be found at <https://www.slicer.org/>. As the software also does a volume rendering of any noise that is present the thresholds needs to be tweaked to remove as much noise as possible without losing too much of the object of interest. Figure 4.12 shows a *Reef knot* and the 3D rendering was done using 800 equidistantly spaced tomographic images created from the projected thickness images, one of them shown in 4.4. This leads to a slightly rougher visual representation but the process is much quicker. Figure 4.13 shows a 3D rendering of a fishing line with a knot. The 3D rendering was done using all 2048 tomographic images, one of which is shown in 4.9.

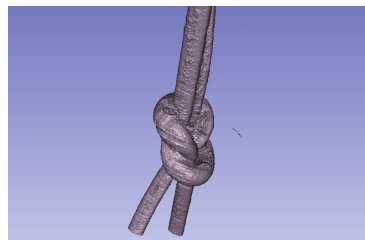


Figure 4.12: 3D rendering of a "reef knot" using the software 3D slicer. The knot is tied using a 100  $\mu\text{m}$  thick fishing line.

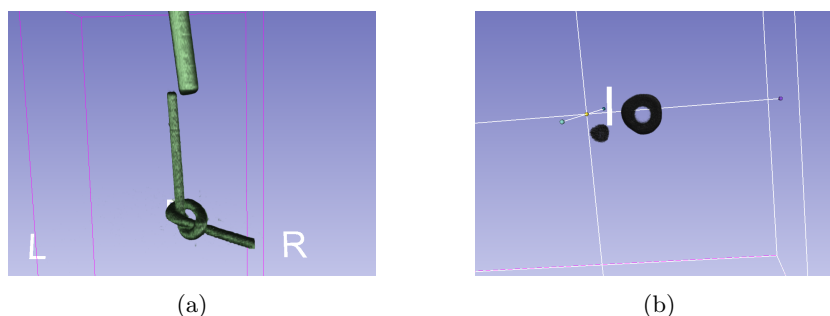


Figure 4.13: These images were created by taking 5 shots at each angle in 5 degree increments from 0 to 180 degrees. A 3D rendering of a simple knot on a 100  $\mu\text{m}$  thick fishing line attached to a dosing needle is shown in (a). The fishing line is not visible at the level of the dosing needle as this blocked most of the intensity during the tomography. (b) shows the same figure rotated, to show it from beneath. The hollow dosing needle is visible despite it being stainless steel and blocking most of the x-rays. The thickness would also not be correct as the algorithm assumes that it is made of mylar, making it thicker than it actually is.

Figure 4.14 shows a 3D rendering of the fly in 3.12, using every 10th image from the tomographic stack of 2048 images, compared to using all 2048. Using all images resolves smaller details better but the process is slow and needs a decent GPU. Figure 4.15 shows a 3D rendering of the upper part of the same fly, cross-section of the head, the end of a leg and a section of the neck. These images were

averaged over 5 shots for each angle and aligned using the automated script.

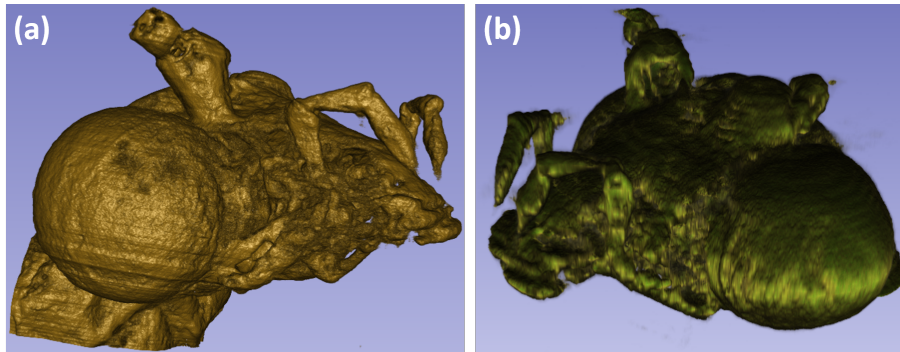


Figure 4.14: Figure (a) was rendered in 3D slicer using all 2048 tomographic images while (b) only used every 10th image. Using more images allows for better resolution, especially for smaller details, which can be seen comparing these two images.

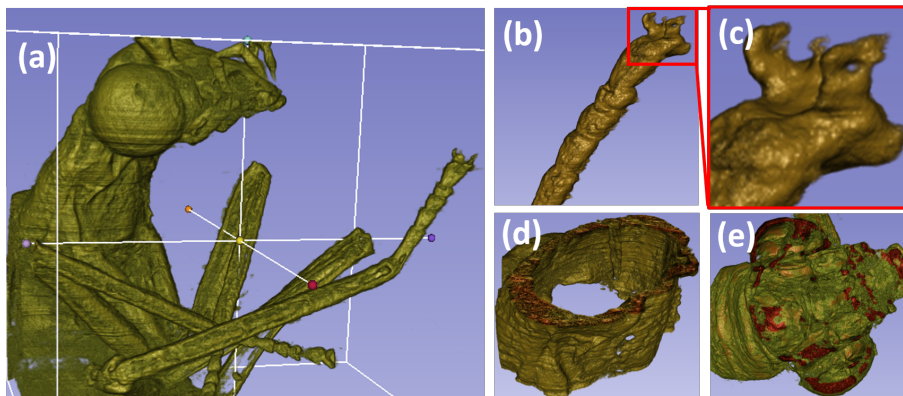


Figure 4.15: 3D rendering of a fly with focus on different parts. The rendering was done for all 2048 images. (a) shows the upper part of the fly and at the bottom of the image one may note that the rendering is not very good. This is due to the poor tomographic reconstruction as part of the fly's back moved outside the frame when rotating. A close-up of the extended leg is shown in (b) with a further zoomed image of the tip shown in (c). The small hooks at the end of the leg can be seen here. Part of the neck was cropped out and is shown in (d) where it can be seen that it is hollow. Figure (e) shows a cut through the head, showing some of the inner structure inside the fly's head, such as some separating walls in the eyes.

At this point it would be possible to do more sophisticated investigations of the sample, such as segmentation of different parts of interest. This has been

excluded as it is not the focus of this thesis but there is a large module library in 3D slicer allowing for such analysis.



## Chapter 5

# Summary and Conclusions

Measurements of the source size in this thesis, show that it is about 2.5 microns vertically and 3.6 microns horizontally, typical values observed in other reports [1], [7], which show source sizes of 4  $\mu\text{m}$  and 1.8  $\mu\text{m}$ . The calculated values are accurate to within 20 % according to [14], leading to a vertical size of approximately  $3.6 \pm 0.72 \mu\text{m}$  and a horizontal size of  $2.5 \pm 0.5 \mu\text{m}$ . This makes the source small enough to be suitable for phase-contrast imaging as it requires a source size on the order of 1 – 10  $\mu\text{m}$ .

The source is asymmetrical which is to be expected and the larger size (horizontal) is in the same direction as the polarization of the laser. This could be explained by the fact that although the electrons oscillate about the optical axis due to the restoring focusing forces of the plasma bubble's walls they also feel the electric field of the laser pulse and this could increase the oscillation amplitude, making the effective source size larger. They would only feel the far end of the tail in the pulse but as the amplitude of the electric field is very large there could be a notable effect. This statement is supported by "Laser-wakefield acceleration of monoenergetic electron beams in the first plasma-wave period" by S.P.D Mangles *et al.* [28] and figure 5.1 is from the same report, showing the electron beam profile at different polarization angles of the laser.

This effect is reported to decrease as the laser pulse made shorter than the plasma wavelength. A shorter laser pulse does not reach as far back in the plasma bubble, resulting in a lower electric field where the electrons are positioned and thus, decreasing this effect. This means that this effect is probably due to the trailing tail of the laser pulse, interacting with the electrons [28].

The implemented algorithm used for phase-retrieval and calculating the projected thickness derived by Paganin *et al.* [21] works as intended and results in good images. It does not fit to the true thickness perfectly, see 4.6, and this is probably due to the low-pass filtering nature of the algorithm. At the edges the function is very sharp, meaning that it is made up of higher frequencies. This can be confirmed to an extent if one takes the true thickness (dashed line in figure 5.2), takes the Fourier transform and applies a low-pass filter. The result is the solid line in figure 5.2 which very much resembles the situation shown in

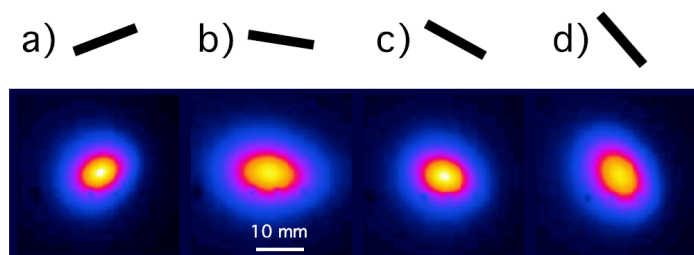


Figure 5.1: Variaton of the electron beam profile for varying polarization angles, visualized be the black lines a)  $-20^\circ$ , b),  $10^\circ$ , c)  $30^\circ$ , d)  $50^\circ$ . The beam looks to be of an elliptical shape and the larger half-axis follows the direction of polarization [28].

figure 4.6, where the edges are smeared.

This also explains why a larger pixel size blurs the image, as shown in figure 3.10, as this limits the highest presentable frequency. Thus, it acts as a threshold for higher frequencies and blur edges in the image. With this insight, the detector becomes an important part of the setup. Making use of as many pixels as possible will be preferable along with having a high resolution detector to get the most accurate value for the projected thickness.

The quality of the images increases as there are more shots to average over. As the current system stands the shots have to be taken manually, with approximately 1 shot / 2 sec, there is a limit to the amount of shots that can be taken within a reasonable time. This repetition rate is mainly limited by the gas injection at the time of writing, as the laser operates at 10 Hz. With an increased repetition rate together with automating the process of taking shots and rotating the sample, the image quality could be greatly improved. This would also decrease the intensity fluctuations between different angles, effectively removing the vertical lines in the sinogram, figure 3.15, for a cleaner image.

The samples chosen were not strictly ideal for this method as they have quite a bit of absorption, not utilizing the technique to its fullest. A very thin sample that absorbs as little as possible to show the usefulness of phase-contrast imaging

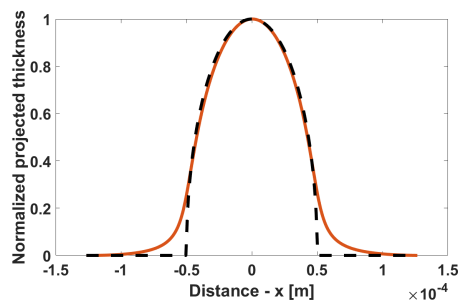


Figure 5.2: Comparison between the exact projected thickness (black dashed line) and a filtered one (orange solid line). The filter was applied in the frequency domain as a low-pass filter, resulting in a blur at the edges.

would be better, alternatively a material surrounded with another material, both having similarly absorption  $\beta$  but different  $\delta$ . These types of samples are usually biological and the difficulty of mounting and preparing them increases as they become smaller/thinner. With more time this is fully realizable. They also need to be dried and processed as to not be destroyed in vacuum.

The phase retrieval algorithm used was Paganin's single material algorithm, equation 2.43 but another phase retrieval method could be used, namely the modified Bronnikov [18]. This does however assume an absorption close to 0 and would not be a good choice for the samples studied here. If a thinner sample was prepared, one might want to investigate further in the effects of source size and polychromaticity for the different methods before making a choice. Another difference between the two algorithms is that Paganin needs knowledge of the refractive index of the sample while Bronnikov does not, which could also influence the choice. This is still a topic of research and better methods might appear in the future, allowing for more flexibility and requiring less prior knowledge.

The optimal distances for phase-contrast imaging in laboratory setups is not trivial to choose and is still a topic of research. In a paper by A. Balles *et al.* [29] published in 2016 they present a way to calculate the optimal distance. For a fixed source-detector distance, this is given by  $r_2 = r_1 \frac{\sigma_p^2 - \sigma_p \sqrt{\sigma_p^2 + \sigma_s^2}}{\sigma_s^2}$ , where  $\sigma_p$ ,  $\sigma_s$  is the standard deviation of the point spread function and the magnified source size respectively. As the point spread function has not been measured, this result was not usable as it is heavily dependant on  $\sigma_p$ . Some estimations were made, but in all cases this resulted in a too low magnification for the samples used here. This was probably due to poor estimations and it could be worthwhile to measure the point spread function to find a more optimized position for the sample to improve the fringe contrast, making the phase-retrieval algorithm to perform better.

The tomographic images shown in figure 4.11 indicate that this source is usable for this application. There are still some artifacts but with a smaller angle increment and more shots per angle this is expected to reduce significantly.

The tomographic reconstruction was done by assuming parallel beam geometry but as the x-ray beam has some divergence this is not fully accurate. This will cause a "tilt" to the sinograms, illustrated in figure 5.3 [22]. A better option would probably be to use a fan beam geometry that assumes a divergent beam instead of a parallel one.

The fan beam geometry have not been discussed in this thesis as this is slightly more complex to implement and due to time constraints a choice was made to use a parallel beam geometry instead, motivated by the fact that the divergence and distances were considered small enough to get a good reconstruction using this geometry. To further improve the results, this should be accounted for.

The experimental setup could also be rearranged to increase the flux. As it currently stands, the CCD camera is mounted on a table outside the chamber with a 1 m tube extending from the chamber towards it. This limits the field of

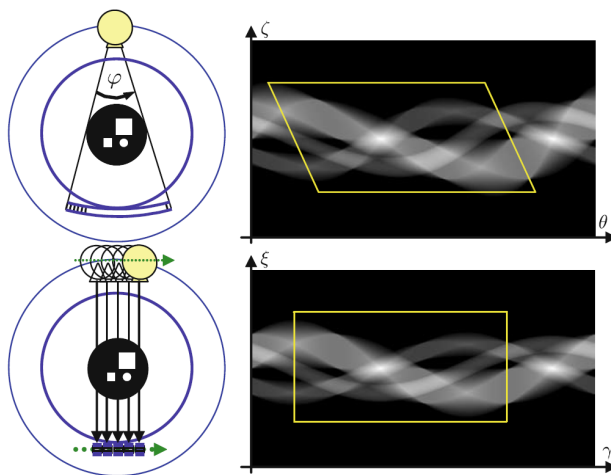


Figure 5.3: Sinogram of a fan beam geometry (top) and a parallel geometry (bottom). The sinogram from a fan beam projection becomes tilted [22].

view for larger magnifications and the need to seal the end of the tube requires the x-rays to pass through a 250  $\mu\text{m}$  thick beryllium window. This reduces the flux and there is another such window mounted on the CCD camera as the chip needs to be cooled in vacuum. Mounting the camera directly to the chamber would allow one to remove one of the windows. The last window is still needed as the CCD needs some protection from the laser but the thickness of it could be reduced since it no longer has to tolerate the vacuum pressure. This would increase the flux as the x-rays no longer have to propagate the 59 mm distance in air and through less beryllium.

One would preferably also use a filter to block the laser and protect the sample if something goes wrong, such as a thin aluminum foil. This was tested in one experiment and worked well, but due to another triggering error it got hit by the full laser power and was destroyed. Using a thicker foil could probably handle this, or a foil that can be moved once it is damaged. The crevices in this foil could clearly be seen and did disturb the image quality somewhat, but it was possible to correct this with some good flat field images as long as the images were aligned.

The energy spectrum was also under some assumptions, assuming it to be synchrotron-like with a critical energy of 3 keV. This was based on previous measurements carried out before the start of this thesis and has not been confirmed here. The outset was to verify the experiment in [1] and to examine the reproducibility of the setup at the laser facility in Lund. From the gathered results it is concluded that it is possible, although there are several improvements that can be made. To further extend this work the temporal duration could be added, as the x-ray pulses are of a very short nature they hold the promise of being able to resolve motion on at least the picosecond scale. This

poses another problem however as these systems are on a micro-scale, requiring massive magnification and there will be a need to focus the x-rays to have an acceptable flux on the sample, which is a difficult task. This would increase the size of the experimental setup significantly and add optical elements, increasing its complexity.

With further improvements to the technique of using LWFA for phase-contrast imaging along with more compact and user friendly laser systems this could one day lead to a reliable table-top source for on-demand phase-contrast imaging of soft tissue materials with very short exposure times resulting in fast data acquisition. It removes the necessity for expensive and limited beam time at synchrotron facilities and would be much faster than currently available microfocus x-ray tubes.

To summarize, the work in this thesis shows that LWFA can be used as an x-ray source for phase contrast imaging, having a source that is small enough, relatively high flux and fast image acquisition. Faster repetition rates will allow for even better contrast as more images can be averaged within a reasonable time and as phase contrast imaging is relatively insensitive to polychromaticity, the full spectrum can be used. The phase contrast images were aligned using an algorithm that makes use of edge detection and the cross-correlation matrix, resulting in pixel-accurate image alignment. Using the phase contrast image to calculate the projected thickness of the samples resulted in images usable for a tomographic reconstruction, which was done for thin fishing lines (100  $\mu\text{m}$  thick), a bee head and a small fly. The tomographic images were then used to do a full 3D volume rendering of the fishing lines and the fly. To summarize and connect to the main goals of this thesis:



# Bibliography

- [1] J. Wenz, S. Schleede, K. Khrennikov, *et al.*, “Quantitative x-ray phase-contrast microtomography from a compact laser-driven betatron source,” *Nature Communications*, vol. 6, p. 7568, Jul. 2015.
- [2] M. Hansson, “Controlled trapping in laser wakefield accelerators,” PhD thesis, Lund University, May 2016.
- [3] W. Leemans, A. Gonsalves, H.-S. Mao, *et al.*, “Multi-GeV electron beams from capillary-discharge-guided subpetawatt laser pulses in the self-trapping regime,” *Physical Review Letters*, vol. 113, no. 24, Dec. 2014.
- [4] MAXIV laboratory: MAXIV guns and linac, [Online]. Available: <https://www.maxiv.lu.se/accelerators-beamlines/accelerators/accelerator-documentation/guns-and-linac/> (visited on 05/15/2017).
- [5] J. Ferri, X. Davoine, S. Kalmykov, *et al.*, “Electron acceleration and generation of high-brilliance x-ray radiation in kilojoule, subpicosecond laser-plasma interactions,” *Physical Review Accelerators and Beams*, vol. 19, no. 10, Oct. 2016.
- [6] G. Genoud, “Laser-driven plasma waves for particle acceleration and x-ray production,” PhD thesis, Lund University, 2011.
- [7] S. Fourmaux, S. Corde, K. T. Phuoc, *et al.*, “Single shot phase contrast imaging using laser-produced betatron x-ray beams,” *Optics Letters*, vol. 36, no. 13, p. 2426, Jun. 2011.
- [8] A. Balerna and S. Mobilio, “Introduction to synchrotron radiation,” in *Synchrotron Radiation*, S. Mobilio, F. Boscherini, and C. Meneghini, Eds., Springer, Jan. 2015. [Online]. Available: [http://dx.doi.org/10.1007/978-3-642-55315-8\\_1](http://dx.doi.org/10.1007/978-3-642-55315-8_1).
- [9] J.-E. Rubensson, *Synchrotron radiation: An everyday application of special relativity*. Morgan & Claypool Publishers, 2016, ch. 3.
- [10] J. M. Cowley, *Diffraction physics*. Elsevier, Dec. 11, 1995, ch. 1. [Online]. Available: [http://www.ebook.de/de/product/5777653/j\\_m\\_cowley\\_diffraction\\_physics.html](http://www.ebook.de/de/product/5777653/j_m_cowley_diffraction_physics.html).

- [11] G. Margaritondo, *Elements of synchrotron light: For biology, chemistry, and medical research*. Oxford University Press, Dec. 11, 2002, pp. 100–101. [Online]. Available: [http://www.ebook.de/de/product/2758558/giorgio\\_margaritondo\\_elements\\_of\\_synchrotron\\_light\\_for\\_biology\\_chemistry\\_and\\_medical\\_research.html](http://www.ebook.de/de/product/2758558/giorgio_margaritondo_elements_of_synchrotron_light_for_biology_chemistry_and_medical_research.html).
- [12] A. Snigirev, I. Snigireva, V. Kohn, *et al.*, “On the possibilities of x-ray phase contrast microimaging by coherent high-energy synchrotron radiation,” *Review of Scientific Instruments*, vol. 66, no. 12, pp. 5486–5492, Dec. 1995.
- [13] A. Peterzol, J. Berthier, P. Duvauchelle, *et al.*, “X-ray phase contrast image simulation,” *Nuclear Instruments and Methods in Physics Research Section B: Beam Interactions with Materials and Atoms*, vol. 254, no. 2, pp. 307–318, Jan. 2007.
- [14] I. N. Tilikin, T. A. Shelkovenko, S. A. Pikuz, *et al.*, “Determination of the size of a radiation source by the method of calculation of diffraction patterns,” *Optics and Spectroscopy*, vol. 115, no. 1, pp. 128–136, Jul. 2013.
- [15] The nobel foundation: The official web site of the nobel prize: The nobel prize in physics 1953, [Online]. Available: [http://www.nobelprize.org/nobel\\_prizes/physics/laureates/1953/](http://www.nobelprize.org/nobel_prizes/physics/laureates/1953/) (visited on 05/15/2017).
- [16] P. Cloetens, “Contribution to phase contrast imaging, reconstruction and tomography with hard synchrotron radiation: Principles, implementation and applications,” PhD thesis, Vrije Universiteit Brussel, European Synchrotron Radiation Facility, 1999.
- [17] A. Momose, “Recent advances in x-ray phase imaging,” *Japanese Journal of Applied Physics*, vol. 44, no. 9A, pp. 6355–6367, Sep. 2005.
- [18] A. Burvall, U. Lundström, P. A. C. Takman, *et al.*, “Phase retrieval in x-ray phase-contrast imaging suitable for tomography,” *Optics Express*, vol. 19, no. 11, p. 10 359, May 2011.
- [19] A. Groso, R. Abela, and M. Stampanoni, “Implementation of a fast method for high resolution phase contrast tomography,” *Optics Express*, vol. 14, no. 18, p. 8103, Sep. 2006.
- [20] D. Paganin, A. Barty, P. J. McMahon, *et al.*, “Quantitative phase-amplitude microscopy. III. the effects of noise,” *Journal of Microscopy*, vol. 214, no. 1, pp. 51–61, Apr. 2004.
- [21] D. Paganin, S. C. Mayo, T. E. Gureyev, *et al.*, “Simultaneous phase and amplitude extraction from a single defocused image of a homogeneous object,” *Journal of Microscopy*, vol. 206, no. 1, pp. 33–40, Apr. 2002.
- [22] T. M. Buzug, *Computed tomography*. Springer Berlin Heidelberg, May 20, 2008, ch. 4. [Online]. Available: [http://www.ebook.de/de/product/8899158/thorsten\\_m\\_buzug\\_computed\\_tomography.html](http://www.ebook.de/de/product/8899158/thorsten_m_buzug_computed_tomography.html).



- [23] J. Hsieh, *Computed tomography: Principles, design, artifacts, and recent advances*. John Wiley & Sons, Jul. 11, 2009, ch. 3. [Online]. Available: [http://www.ebook.de/de/product/8945459/jiang\\_hsieh\\_computed\\_tomography\\_principles\\_design\\_artifacts\\_and\\_recent\\_advances.html](http://www.ebook.de/de/product/8945459/jiang_hsieh_computed_tomography_principles_design_artifacts_and_recent_advances.html).
- [24] B. Henke, E. Gullikson, and J. Davis. The center for x-ray optics: X-ray interactions with matter, [Online]. Available: [http://henke.lbl.gov/optical\\_constants/](http://henke.lbl.gov/optical_constants/) (visited on 05/15/2017).
- [25] Mathworks: Rapezoidal numerical integration - MATLAB trapz, [Online]. Available: <https://se.mathworks.com/help/matlab/ref/trapz.html> (visited on 05/15/2017).
- [26] L. Edsberg, *Introduction to computation and modeling for differential equations*. John Wiley & Sons, Oct. 5, 2015, ch. 3. [Online]. Available: [http://www.ebook.de/de/product/24211694/lennart\\_edsberg\\_introduction\\_to\\_computation\\_and\\_modeling\\_for\\_differential\\_equations.html](http://www.ebook.de/de/product/24211694/lennart_edsberg_introduction_to_computation_and_modeling_for_differential_equations.html).
- [27] U. Lundström, “Phase-contrast x-ray carbon dioxide angiography,” PhD thesis, KTH Royal Institute of Technology, 2014.
- [28] S. P. D. Mangles, A. G. R. Thomas, M. C. Kaluza, *et al.*, “Laser-wakefield acceleration of monoenergetic electron beams in the first plasma-wave period,” *Physical Review Letters*, vol. 96, no. 21, May 2006.
- [29] A. Balles, S. Zabler, T. Ebersperger, *et al.*, “Propagator based formalism for optimizing in-line phase contrast imaging in laboratory x-ray setups,” *Review of Scientific Instruments*, vol. 87, no. 9, p. 093707, Sep. 2016.